



Satellite-observed surging dynamics of North Kunchhang Glacier I in the Eastern Karakoram

Fanyu Zhao^{1,2}, Di Long^{1,2,4}, Chenqi Fang^{1,2}, Yiming Wang^{1,2}, and Xingwu Duan^{3,4}

¹State Key Laboratory of Hydrosphere and Engineering, Department of Hydraulic Engineering, Tsinghua University, Beijing, 100084, China

²Key Laboratory of Hydrosphere Sciences of the Ministry of Water Resources, Tsinghua University, Beijing, 100084, China

³Institute of International Rivers and Eco-security, Yunnan University, Kunming, 650091, China

⁴Southwest United Graduate School, Kunming, 650092, China

Correspondence to: Di Long (dlong@tsinghua.edu.cn)

10 **Abstract.** Frequent glacier surges are a distinctive characteristic of Karakoram glaciers, with their increased occurrence profoundly impacting glacier morphology and dynamics. However, limited and short-term observations have constrained our understanding of surging dynamics and their underlying mechanisms. This study employs extensive multisource remote sensing data to investigate long-term, multi-phase changes in flow velocity, surface elevation, and terminus position of North Kunchhang Glacier I (NKG I) in the Eastern Karakoram. By examining 25 years of changes, we identified the timing of glacier surges, estimated mass transfer during surging events, and analysed spatiotemporal correlations among key variables. Historical interpretation of terminus dynamics dating back to 1972 revealed a prior main trunk surge around 1980, enabling an exploration of potential climate change impacts on surge behaviour. Our results indicate that the 2017 main trunk surge lasted four years (June 2015–June 2019), transferring ~ 0.45 Gt of glacier mass, inducing significant downstream elevation gain, and leading to a delayed terminus advance starting in 2018, three years after the surge initiation. In contrast, the 2004 surge of NKG V (within the NKG basin and connected to NKG I after surge) lasted 2.5 years (November 2002–April 2005), transferring ~ 0.23 Gt of glacier mass, destroying a proglacial lake, and raising its surface elevation by ~ 180 m. Flow velocity, surface elevation, and terminus position derived from various sources exhibit strong consistency in both trends and values, confirming the reliability of our results. Notably, the 2017 surge exhibited a shorter rapid advance period compared to the 1980 surge, suggesting that climate change may be influencing surge mechanisms, leading to smaller-scale but more frequent events. These findings provide new insights into the surging dynamics of NKG I and contribute to a deeper understanding of Karakoram glacier behaviours. The integration of multisource remote sensing demonstrates its critical value in deciphering complex glacier dynamics and their responses to a changing climate.



1 Introduction

Frequent glacier surges and slight mass gains are defining characteristics of Karakoram glaciers (Farinotti et al., 2020; Bazai et al., 2021), collectively known as the Karakoram Anomaly (Hewitt, 2005; Berthier and Brun, 2019; Bolch et al., 2012). Glacier surges are periodic events marked by a rapid acceleration in flow velocity following a long-term quiescent phase, during which the velocity can speed up to 10 to 100 times of the normal (Guo et al., 2022). Glaciers exhibiting such behaviour are referred to as surge-type glaciers. Notably, 12.6% of the 150 glaciers in the central Karakoram are surge-type (Barrand and Murray, 2006), a percentage significantly higher than that observed elsewhere in High Mountain Asia (HMA), such as the Himalayas, Tien Shan, Kunlun Shan, and Southeastern Tibetan Plateau. Although the Karakoram region contains only 181 surge-type glaciers, these glaciers collectively cover nearly 10,000 km², accounting for 51% of the total area of surge-type glaciers across HMA (Leclercq et al., 2021; Pfeffer et al., 2014).

Glacier surges involve a dramatic redistribution of ice and moraines, transferring mass from the reservoir area to the receiving area. This process leads to significant surface elevation changes and can result in terminus advance of several kilometres. For instance, the surge of the Kutiah Glacier in Pakistan caused a remarkable 12 km terminus advance within three months in 1953 (Bhambri et al., 2017). Surges also create distinct geomorphic features, such as looped and folded moraines and widespread surface crevasses, transforming glacier morphology. These events pose significant risks to downstream communities by triggering natural disasters, including catastrophic floods, ice avalanches, and glacier-induced debris flows (Bazai et al., 2021; Guo et al., 2022). Therefore, understanding the dynamics and mechanisms of glacier surges is critical not only for advancing glaciological science but also for improving disaster risk management in vulnerable regions.

The initiation and dynamics of glacier surges are governed by a complex interplay of factors, including the mass-energy balance, englacial and subglacial thermal regimes, hydrological processes, and basal conditions (Crompton et al., 2018; Guo et al., 2022). Surges in the Karakoram cannot be solely explained by either hydrological control mechanisms (Quincey et al., 2015; Gao et al., 2024), as observed in Alaska's Variegated Glacier (Kamb et al., 1985), or by thermal control mechanisms, as seen in the Trapridge Glacier in Canada (Clarke et al., 1984). This heterogeneity highlights significant gaps in our understanding of glacier surging dynamics in the region (Wu et al., 2020), emphasizing the need for detailed studies to better elucidate the underlying processes.

Remote sensing has emerged as an indispensable tool for studying glacier surges due to its ability to capture dramatic changes in surface morphology and dynamics over large spatial and temporal scales (Guo et al., 2022). For instance, satellite imagery can identify surge-type glaciers based on changes in length or surface features (Wytiahlowsky et al., 2023), while image cross-correlation feature-tracking techniques enable monitoring of glacier velocity (Zhang et al., 2024; Li et al., 2024). Additionally, digital elevation model (DEM) differencing provides insights into surface elevation changes (Wu et al., 2021; Brun et al., 2017; Zhao et al., 2022). However, remote sensing studies are often limited by temporal coverage, sensor capabilities, or reliance on specific data types, which can lead to incomplete assessments of surface processes.



60 In this study, we utilize a multisource remote sensing approach to investigate the surging dynamics of North Kunchhang
Glacier I (NKG I) in the eastern Karakoram. By combining multiple data types and analysis techniques, we aim to capture
long-term and continuous changes in glacier flow velocity, surface elevation, terminus position, and glacial lake levels
during different surge stages. Specifically, we analyse glacier flow velocity using the ITS_LIVE dataset to identify the
timing and extent of the surges, examine surface elevation changes using satellite altimetry and DEMs, and track terminus
65 position changes using a newly developed algorithm applied to Sentinel-1 Single Look Complex (SLC) images. Additionally,
we analyse longer-term terminus changes using historical Landsat and KH-9 imagery, and assess lake level variations in a
newly formed ice-dammed lake.

By integrating these time-series datasets, we provide a detailed overview of the evolution of NKG I during its surge cycles,
focusing specifically on the spatiotemporal correlations among key variables. Compared to previous studies, our multisource
70 remote sensing approach offers a more comprehensive understanding of surge dynamics, emphasizing the
interconnectedness of flow velocity, elevation, terminus position, and lake level changes. This study not only enhances our
understanding of NKG I's surging dynamics but also provides valuable insights into the mechanisms driving glacier surges
in the Karakoram region.

2 Study area and data

75 2.1 Study area

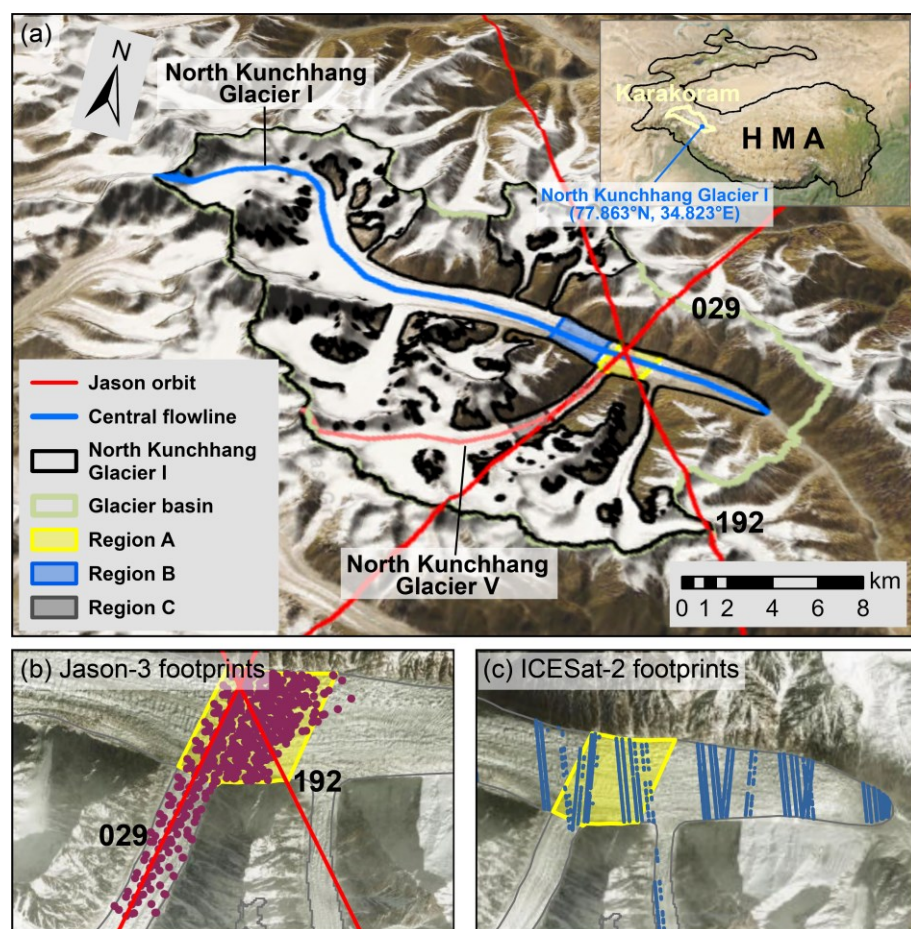
The Karakoram, located in the western HMA, is characterized by its rugged topography and abundance of towering peaks
exceeding 7,000 m. This region boasts some of the most extensive and well-developed mountain glaciers in mid-to-low
latitudes (Kumar et al., 2019; Xie et al., 2023), with glaciers covering approximately 25.6% of its area. It encompasses
11,586 glaciers, including 278 that each span more than 10 km². The total glacierized area is 21,475 km², representing 22%
80 of the glacierized area in HMA (Pfeffer et al., 2014). The Karakoram contains a glacier volume of 3,411 km³, accounting for
31% of HMA's total glacier volume (Millan et al., 2022). Notably, the Karakoram ranks second in the number of surge-type
glaciers and first in the total area of these glaciers within HMA (Guo et al., 2022). This makes the region a critical hotspot
for studying glacier surges, offering unique insights into glacier dynamics and behaviour under the influence of a rapidly
changing climate.

85 North Kunchhang Glacier I (NKG I, RGI60-14.08555) is situated in the Eastern Karakoram at central coordinates 77.863°N,
34.823°E (Fig. 1). Following the surge of North Kunchhang Glacier V (NKG V, RGI60-14.08634) around 2004, NKG V
advanced and connected with the main trunk of NKG I. For this study, the two glaciers are treated as a single glacier system
with a total area of 182.5 km², making it the 21st largest glacier in HMA (Pfeffer et al., 2014). The highest peak of the glacier
system is Saser Kangri I, which reaches an elevation of 7,672 m, while its terminus lies at 4,712 m. NKG I is a large
90 dendritic valley glacier, flowing predominantly from west to east. It is a typical surge-type glacier, characterized by



pronounced looped moraines. The region has a mean annual precipitation of approximately 500 mm (1950–2024) (Muñoz-Sabater et al., 2021). The steep slopes in its reservoir area make the glacier highly susceptible to avalanches and associated hazards.

From a data availability perspective, NKG I's wide main trunk intersects with two Jason ground tracks, providing valuable satellite altimetry data. Historical records indicate multiple surges in different sections of NKG I over the past few decades (Yang et al., 2021), including a major surge of the southern NKG V around 2004 and a significant surge of the main trunk around 2017. These events are well-captured by satellite observations, making NKG I an ideal natural laboratory for investigating glacier surge dynamics using remote sensing techniques.



100 **Figure 1: Location of NKG I and footprints of Jason-3 and ICESat-2.** Panel (a) shows the central flowlines of NKG I (blue) and NKG V (coral), which are used for analysing surface velocity and elevation. The red lines represent the ground tracks of Jason-3. Region A marks the section of the main trunk intersected by Jason-3 footprints, while Regions B and C highlight the areas with the fastest velocities during the surges of the main trunk and the tongue of NKG V, respectively. The inset in the upper-right corner of (a) illustrates the location of HMA, the Karakoram, and NKG I. Panels (b) and (c) present the detailed footprints of Jason-3 and ICESat-2 on NKG I,



105 respectively. The basemaps in panels (a), (b), and (c) are derived from ESRI World Imagery and Hillshade (Credits: Esri, NASA, NGA, USGS, Earthstar Geographics, Sources: Esri, TomTom, Garmin, FAO, NOAA, USGS, © OpenStreetMap contributors, and the GIS User Community).

2.2 Data and tools

This study integrates a diverse array of multisource remote sensing datasets to investigate the surging dynamics of NKG I, encompassing satellite altimetry, optical and Synthetic Aperture Radar (SAR) images, DEMs, glacier velocity maps, glacier inventories, and climate reanalysis data. To analyse annual and monthly glacier velocity changes, 6,260 maps from the ITS_LIVE dataset (Nilsson et al., 2023) were used. These maps were derived using autoRIFT (Lei et al., 2021) from Landsat 5/7/8/9, Sentinel 1A/B, and Sentinel 2A/B imagery. Glacier surface elevation changes were extracted from Jason-3 close-loop mode altimetry data (Ray et al., 2024) and ICEat-2 Land Ice Height data (ATL06) (Smith, 2020). Additionally, 137
115 ASTER DEMs spanning 2000 to 2019 (Hugonnet et al., 2021) and a GF-7 DEM in 2024 were utilized to reconstruct elevation time series for glacier and proglacial lake surfaces. NASADEM (Crippen et al., 2016), reflecting glacier conditions in 2000, served as the reference DEM, while the Randolph Glacier Inventory (RGI) 6.0 (Pfeffer et al., 2014) was used as the reference glacier mask.

This study also leveraged 1,238 Sentinel-1 SLC image pairs collected since 2014 to map glacier extents and terminus
120 positions with high temporal resolution. To supplement these datasets, manual delineation of NKG I's terminus since 1972 was performed using 36 cloud-free Landsat 5/7/8/9 images captured during summer months (June and September), three Landsat 1/2/3 Multispectral Scanner (MSS) images, and four KH-9 images (Surazakov and Aizen, 2010; Zhou et al., 2017). In addition, three Sentinel-1A Ground Range Detected (GRD) images facilitated the identification of glacial lakes. To explore the climatic drivers influencing glacier surges, ERA5-Land monthly aggregated data (Muñoz-Sabater et al., 2021) on
125 temperature, precipitation, and radiation were analysed.

For data processing, various advanced tools were employed. The Python package PyFlwDir (<https://deltares.github.io/pyflwdir/latest/index.html>) was utilized to delineate the NKG basin and vectorize binary coherence maps. A Fast Time-Series InSAR Processing Software (ESIS) (Yu et al., 2024) and the Alaska Satellite Facility's Hybrid Pluggable Processing Pipeline (ASF Hyp3) service (<https://hyp3-docs.asf.alaska.edu/>) were used to estimate the coherence
130 of Sentinel-1 image pairs. This comprehensive dataset and associated tools provided a robust foundation for investigating the surging behaviour, kinematics, and underlying climatic drivers of NKG I. A detailed summary of the datasets and tools is provided in Table 1.



Table 1 Detailed information on data and tools used in this study

Category	Data	Time span	Sensor	Spatial resolution	Temporal Resolution	Purpose	Data Source
Satellite altimetry	Jason-3 SGDR-F	2016–2020 (close loop mode)	Poseidon-3B	~ 330 m along-track	10 d	Surface elevation retrieval	AVISO (ftp://ftp-access.aviso.altimetry.fr/)
	ICESat-2 ATL06	2018–present	ATLAS	20 m	91 d		NSIDC (https://nsidc.org/data/atl06/version/6)
Optical image	KH-9	1971–1984	Telescopic camera system	6–9; 0.6–1.2 m	*	Glacier terminus mapping	EarthExplorer (https://earthexplorer.usgs.gov/)
	Landsat 1/2/3/5/8/9 Collection2 Level 1	1972–present	MSS, TM, ETM+, OLI, and OLI-2	60 / 30 m	16 d		GEE (https://developers.google.com/earth-engine/datasets/)
	Sentinel-2A/B	2015–present	MSI	10 m	5 d	Reference image	EarthExplorer (https://earthexplorer.usgs.gov/)
	GF-7 DLC	2019–present	Dual-line-array camera	0.65 m (BWDPAN); 0.8 m (FWDPAN)	≤ 60 d	DEM generation	By purchase; Acquisition time: 2024.07.16
SAR image	Sentinel-1A/B IW GRD	2014–present	C-SAR	20 m	12 d	Glacial lake extent retrieval	ASF (https://search.asf.alaska.edu/)
	Sentinel-1A/B IW SLC			5 × 20 m		Glacier extent retrieval	
Other datasets	ITS_LIVE	1985–present	*	120 m	0–500 d	Surface velocity retrieval	JPL (https://its-live.jpl.nasa.gov/)
	ASTER DEM	2000–2019	*	100 m	0–336 d	Surface elevation retrieval	SEDOO (https://doi.org/10.6096/13); Github (https://github.com/rhugonnet/ww_tvol_study)
	NASADEM	2000	*	30 m	*	Reference DEM	Earthdata Search (https://doi.org/10.5067/MEaSUR-Es/NASADEM/NASADEM_HG_T.001)
	Copernicus DEM	2011–2015	*	30 m	*	Surface elevation retrieval	OpenTopography (https://opentopography.s3.sdsc.edu/minio/raster/COP30/)



	RGI 6.0	2002 (NKG I)	*	*	*	Reference glacier mask	GLIMS (https://www.glims.org/RGI/ranoloph60.html)
	ERA5-Land Monthly Aggregated	1950– present	*	0.1 °	Monthly	Attribute analysis	GEE (https://developers.google.com/earth-engine/datasets/catalog/ECMWF_ERA5_LAND_MONTHLY_AGGREGATED)
Tool and service	PyFlwDir	A Python package contains a series of methods to work with gridded DEM and flow direction datasets				Glacier basin delineation and glacier vectorization	Github (https://deltares.github.io/pyflwdir/latest/)
	ESIS	A Fast Time-Series InSAR Processing Software				Sentinel-1 coherence estimation	Notion (https://southern-saxophone-c79.notion.site/ESIS-28bb22a6db2c4043a099ae3fb3959685)
	ASF Hyp3	Alaska Satellite Facility's Hybrid Pluggable Processing Pipeline					ASF (https://hyp3-docs.asf.alaska.edu/)

* denotes that this attribute is not applicable to the data.

3 Methodology

135 This study analyses multisource remote sensing data to derive critical information on flow velocity, surface elevation, glacier extent, terminus position, and glacial lake level before, during, and after surging events. To achieve this, extensive data processing steps were undertaken, as detailed below.

3.1 Processing of ITS_LIVE glacier velocity data

140 A total of 6,260 glacier velocity maps were downloaded using the ITS_LIVE API. These velocity maps, generated from optical and radar image pairs (Landsat 5/7/8/9, Sentinel-1A/B, and Sentinel-2A/B) using the autoRIFT algorithm, were selected with time intervals between image acquisitions not exceeding 90 days. During the preliminary analysis, it was observed that excessively short intervals led to significant velocity fluctuations, while longer intervals often resulted in underestimated velocities. To address this, only data with time intervals ranging from 2 to 45 days were retained for the final analysis, ensuring more reliable velocity estimates.

145 Give that the ITS_LIVE dataset does not always provide complete spatial coverage of NKG I, we aggregated the data to annual and monthly timescales to calculate mean glacier velocities for each period. This approach enabled us to investigate the spatiotemporal characteristics of glacier velocity in detail. Additionally, focused analyses were conducted in regions of interest, including: Region A, which overlaps with Jason-3 footprints and serves as a key area for surface elevation analysis,



and Regions B and C, where the highest glacier velocities were observed during surge periods, representing the main trunk
150 of NKG I and tongue of NKG V, respectively. By combining spatial and temporal aggregation with targeted regional
analyses, we captured velocity changes across NKG I throughout the surging process.

3.2 GF-7 DEM generation and ASTER DEM processing

A stereo image pair from the GF-7 satellite, acquired on July 16, 2024, was utilized to generate a high-resolution DEM.
Using the rational function model, 10 ground control points and 28 tie points were manually selected in PCI Geomatica for
155 accurate geometric correction. The resulting DEM was resampled to a 30-m spatial resolution and co-registered to
NASADEM using Nuth and Kaab (2011)'s approach. In addition to the GF-7 DEM, 137 ASTER DEMs (Hugonnet et al.,
2021) spanning 2000 to 2019 were employed to construct a surface elevation time series for various regions, including
Regions A, B, and C. ASTER DEMs were first filtered based on valid value coverage and cross-referenced against
elevations derived from NASADEM, Copernicus DEM, and GF-7 DEM to identify and exclude low-quality or anomalous
160 data. A threshold of 200 m was applied to account for significant elevation changes associated with surging events, ensuring
robust data selection. All DEMs were converted to the EGM96 vertical reference to maintain consistency across datasets.
High-quality DEMs from pre- and post-surge periods were analysed separately to estimate mass transfer during the surges.
Additionally, surface elevations along central flowlines and cross-sectional profiles were extracted from selected DEMs to
quantify elevation changes and derive insights into the redistribution of glacier mass.

165 3.3 Altimetry data processing

Jason-3 is designed to produce global sea surface height measurements every 10 days with an accuracy better than 4 cm
(Biancamaria et al., 2018). For observing inland water bodies, ice sheets, or mountain glaciers, 20 Hz data and waveform
retracking are essential. Figures 2a and 2b illustrate the altimeter signals over glacier and glacial lake surfaces, respectively.
The glacier surface elevation at the footprint of the altimeter radar pulse is calculated as follows (Hwang et al., 2021):

$$170 \quad H_g = Alt - Range - Cor - H_{geoid}, \quad (1)$$

where H_g is the glacier surface elevation above mean sea level (m. s. l), Alt is the Jason-3 altimeter ellipsoid height above the
WGS84 ellipsoid, $Range$ is the radar range measurement, and H_{geoid} is the geoid height relative to the WGS84 ellipsoid. The
correction term Cor contains multiple components:

$$Cor = C_{wet} + C_{dry} + C_{iono} + C_{solid} + C_{pole} + C_{retrack}, \quad (2)$$

175 where C_{wet} , C_{dry} , C_{iono} , C_{solid} , and C_{pole} are corrections for wet tropospheric delay, dry tropospheric delay, ionosphere delay,
solid Earth tide, and pole tide, respectively, all of which are provided in the Jason-3 SGDR-F dataset. The $C_{retrack}$ term is the
radar range correction by waveform retracking. In this study, we employed the threshold retracking method with a 50%
threshold value (Hwang et al., 2021). Jason-3 waveforms consist of 104 gates, with the default gate being 32.5. The $C_{retrack}$



value is computed as the difference between the default gate and the retracked gate, multiplied by a gate-to-meter factor
 180 (0.46875 m). Our analysis revealed that only a limited number of radar waveforms could be retracked to improve altimetry-
 derived glacier surface elevations in Region A (Fig. 1).

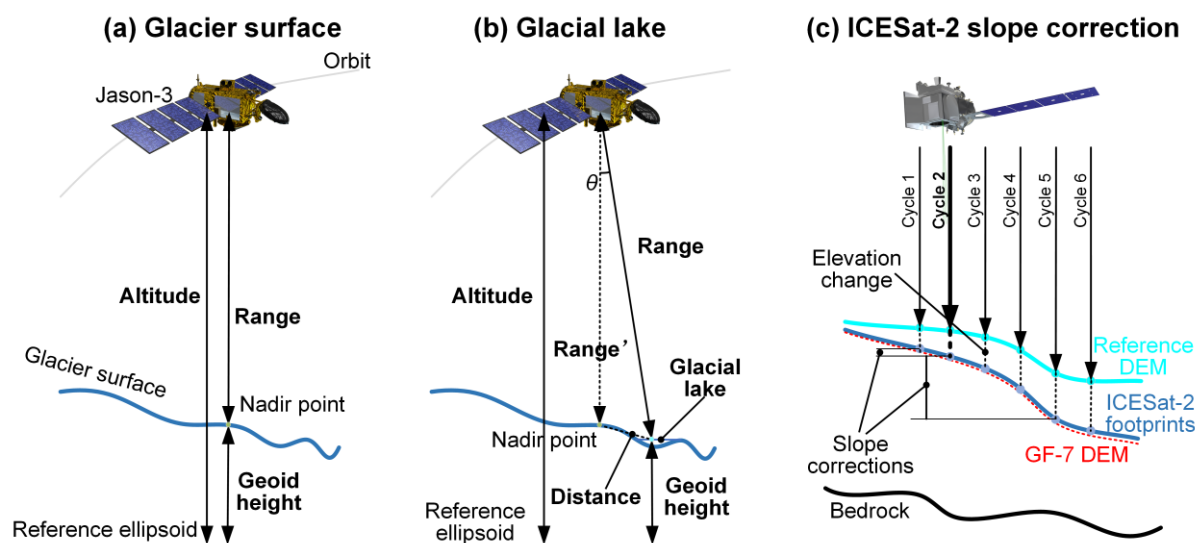


Figure 2: (a) Altimeter signals over the glacier surface. (b) Altimeter signals over the glacial lake surface. (c) Schematic diagram of
 ICESat-2 observations on the glacier surface. The blue lines represent glacier surface profiles at different times, while the red dashed line
 185 depicts the glacier surface derived from the GF-7 DEM acquired on Jul 16, 2024. The vertical dashed lines in (c) indicate potential
 elevation differences observed across various observation cycles.

After waveform retracking, we filtered out outliers by cross-referencing NASADEM, Copernicus DEM, and GF-7 DEM,
 along with waveform amplitude and shape characteristics. The time series of mean glacier surface elevations for Region A
 was obtained by averaging all glacier elevations for each cycle. However, given Jason-3's large footprint, some recorded
 190 elevations in Region A were influenced by the tongue of NKG V. To address this, we divided the time series into two
 subsets based on the distinct elevation trends of the main trunk and the glacier tongue of NKG V. After bias correction, these
 two subsets showed strong agreement with both DEM and ICESat-2 elevation time series.

During outlier removal, we identified 177 footprints with anomalously low elevations compared to the reference DEMs.
 These footprints exhibited strong radar signals with waveform shapes typical of inland water bodies, such as narrow rivers or
 195 small lakes smaller than the altimeter footprint. Upon further examination, we determined that these low elevations
 corresponded to the water level of a small ice-dammed lake located approximately 1.2 km downstream of Region A. This
 phenomenon arises because the radar signal reflected from water surfaces is significantly stronger than from glacier or land
 surfaces. When the glacial lake is sufficiently large, the radar signal primarily captures the adjacent lake surface rather than
 the glacier surface at the nadir point.



200 However, these elevations correspond to non-nadir reflections, necessitating additional corrections to ensure accuracy. Considering the possibility of glacial lake freezing (Li et al., 2021; Li et al., 2023), we modified the waveform retracking threshold to 10%. Non-nadir correction values were calculated as follows:

$$C_{non-nadir} = Range * (1 - \cos \theta) \approx Range - \sqrt{Range^2 - d^2}, \quad (3)$$

where θ is the angle of incidence and d is the distance between the nadir point and the glacial lake. Consequently, the
205 correction term Cor for glacial lake elevations in Eq. (1) is updated as:

$$Cor = C_{wet} + C_{dry} + C_{iono} + C_{solid} + C_{pole} + C_{retrack} + C_{non-nadir}, \quad (4)$$

For ICESat-2 observations, the mean elevation of all footprints within each cycle was calculated. However, due to the 1.5-
km width of Region A and the combined influence of glacier surface slope, movement, and ablation, substantial
discrepancies were observed in elevation measurements at different locations and times. These discrepancies were
210 particularly evident in high-spatial-resolution ICESat-2 data (Fig. 2c).

We then applied slope corrections to the ICESat-2 data. To minimize the influence of glacier movement and ablation on the
slope correction, we selected the GF-7 DEM, which is temporally aligned with ICESat-2 observations. A relationship
between longitude and elevation along the central flowline in Region A was modelled using a third-order polynomial.
Expected elevations of a specific cycle was computed from the mean longitude of that cycle. The slope correction for a
215 specific cycle was then calculated by subtracting the reference cycle elevation from the expected elevation:

$$C_{slope} = Ele_{lon} - Ele_{lon_0} = f(lon) - f(lon_0), \quad (5)$$

where lon is the mean longitude of a specific cycle, and lon_0 is the reference cycle longitude. Ele_{lon} and Ele_{lon_0} are expected
elevations of the specific cycle and the reference cycle, respectively. f is the fitted third-order polynomial.

3.4 Glacier extent and terminus position extraction

220 Accurate mapping of glacier extent using optical images, such as Landsat or Sentinel-2, is often hindered by the presence of
thick moraines on glacier tongues (Lin et al., 2023) and frequent cloud cover. Alternatively, SAR imagery provides an
effective solution, as the coherence of SAR image pairs is notably lower over glaciers compared to surrounding terrain due
to glacier flow (Shi et al., 2019). SAR satellites also have advantage of being unaffected by cloud cover and can operate
during nighttime, making them particularly suitable for monitoring glacier changes. Leveraging multitemporal SAR
225 coherence maps offers a practical approach for tracking glacier extent and terminus position changes. However, SAR
imagery is subject to challenges. Issues such as foreshortening, layover, shadowing, and salt-and-pepper noise in
mountainous regions can introduce errors in delineating glacier extents. To mitigate these challenges, we employed a new
approach utilizing both ascending and descending Sentinel-1 SLC images. This strategy effectively reduces the impact of
SAR imaging artifacts and enables the accurate extraction of glacier terminus positions and extents at high temporal



230 resolution. Given the high sensitivity of SAR coherence to surface changes, this method has additional potential for applications such as detecting small water bodies, wetlands, and snow cover with minor modifications.

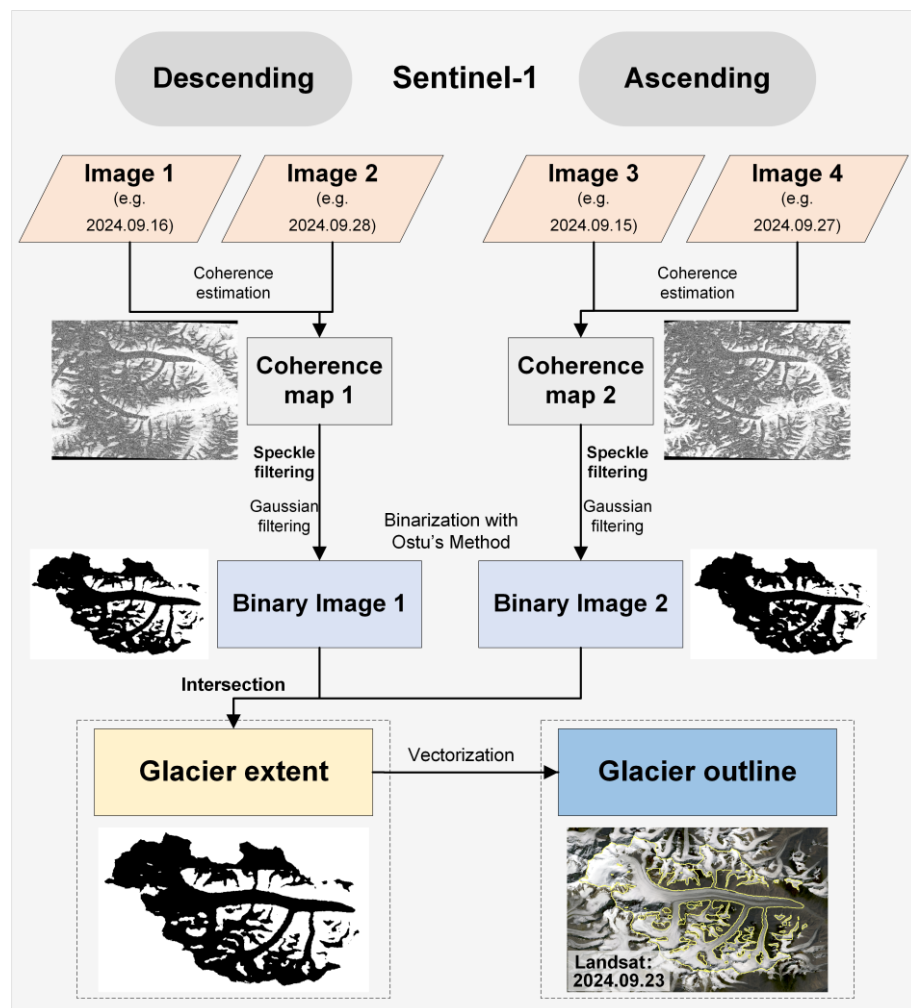


Figure 3: Flowchart for extracting glacier outlines using Sentinel-1 SLC images. The basemap of the glacier outline is a Landsat 8 image acquired on September 23, 2024.

235 Since glacier extents over time may differ from those in RGI 6.0, we processed all relevant data within the NKG basin, ultimately focusing our analysis on the NKG I glacier. The basin was delineated using the PyFlwDir tool and NASADEM. Figure 3 illustrates the workflow for extracting glacier extents using Sentinel-1 imagery. Initially, we performed coherence estimation on image pairs of descending and ascending passes acquired within similar timeframes (typically 12 days apart). Using the ESIS tool and the ASF HyP3 service, we generated two sets of coherence maps. To reduce salt-and-pepper noise, we applied speckle filtering (Aja-Fernández and Alberola-López, 2006) followed by Gaussian filtering to the coherence maps. These filtered maps were then binarized using Otsu's method (Otsu, 1979). The binary maps from ascending and

240

descending passes were intersected to generate the final glacier extent corresponding to the acquisition time of the descending image. Lastly, the binary image was vectorized using the PyFlwDir tool to produce glacier outlines.

245 Due to data gaps during specific periods, we derived 184 glacier outlines representing various time points, with annual counts ranging from 3 to 25 since 2014. After obtaining these outlines, we extended the central flowline of NKG I and extracted its intersection points with the glacier outlines to determine terminus positions at different times. To further capture long-term changes in the terminus position of NKG I, we manually mapped terminus positions using both Landsat images and declassified KH-9 images, enabling us to extend the analysis back to 1972. To ensure consistency, the KH-9 images were georeferenced to the Landsat images. This comprehensive approach allowed us to document terminus position changes
250 over five decades, providing critical insights into historical glacier dynamics.

3.5 Glacial lake level and drainage analysis

Over the past few decades, two ice-dammed lakes have formed in the NKG I region. The first glacial lake, a proglacial lake of NKG V, disappeared at the end of 2004 due to the surge of NGK V. Its extent was manually delineated based on a Landsat 7 image acquired on July 20, 2003. The second glacial lake emerged when the main trunk blocked the meltwater
255 outlet of a tributary glacier and NKG V, located approximately 1.2 km downstream of Region A. This lake is relatively small and our Jason-3 results observed an abrupt decrease in its lake level during summer 2018. To investigate the abrupt level decrease, we manually delineated the lake's outlines from July to October 2018 using a combination of Landsat 8, Sentinel-2, and Sentinel-1 GRD images. Additionally, we selected a representative cross-section near the lake's outlet on the main trunk and extracted elevations along this cross-section from multiple sources, including NASADEM, ASTER DEMs, and GF-7
260 DEM, spanning different time periods.

3.6 Uncertainty analysis

The ITS_LIVE dataset, known for its low latency and high consistency across satellite -derived velocity estimates (López et al., 2023), was integral to this study. Of the 6,260 velocity maps available for the NKG region, 3,295 met our selection criteria. Among these selected velocity maps, those derived from Landsat 8, Sentinel-1A, and Landsat 7 covered a period of
265 over 10 years, accounting for 17.8%, 15.0%, and 13.4% of the total, respectively. To evaluate the consistency of glacier velocity measurements, we conducted point-scale comparisons of time series from these three sources. The results showed high consistency in both peak velocities and overall trends. Furthermore, Fourier transform analysis revealed that the amplitude similarity between the three pairs of time series exceeded 0.88, indicating minimal differences in flow velocity estimates from Landsat 7/8 and Sentinel-1A. By averaging velocity maps over specific time periods, we improved spatial
270 coverage and reduced uncertainty in the glacier velocity estimates.

For glacier surface elevation and glacial lake levels, we minimized fluctuations by applying spatial averaging. Moreover, elevations derived from various datasets, including ASTER DEM, GF-7 DEM, Jason-3, and ICESat-2, exhibited high



consistency. Cross-validation between these datasets confirmed the reliability of our elevation estimates. To quantify
uncertainties in elevation change rates, we performed piecewise linear regression on the elevation time series. The standard
275 deviation of the regression slopes was used to represent the uncertainty for each assessed period.

Regarding glacier extent, glacier outlines derived from Sentinel-1 images demonstrated strong agreement with visually
interpreted outlines from Landsat images for similar time periods. For terminus position analysis, we accounted for potential
errors introduced by differences in spatial resolution between data sources, estimating these errors to be less than half a grid
cell. Despite these potential discrepancies, the multi-year trends in terminus changes, whether advancing or retreating, were
280 consistent and clearly discernible. Additionally, trends observed in visually interpreted terminus position changes aligned
with those identified through automated detection methods, further validating our approach and results.

4. Results

4.1 Glacier surges and surface velocity dynamics

To analyse glacier surges and their associated velocity variations, we averaged the 3,295 velocity maps that met our selection
285 criteria to derive annual mean velocities for NKG I from 2000 onward. This analysis revealed two major glacier surges,
along with several smaller rapid motion events over the past 25 years (Fig. 4). The first surge occurred between 2003 and
2005, primarily affecting NKG V. During this period, glacier velocity peaked in 2004, exceeding 1,700 m/yr. However, this
surge had minimal impact on the main trunk of NKG I, with the affected regions mainly confined to NKG V and the ice-
dammed lake in front of it. The second surge, occurring between 2016 and 2018, was significantly larger in scale, centered
290 on the main trunk of NKG I. The peak velocity was recorded in 2017, with an annual mean velocity of around 600 m/yr.

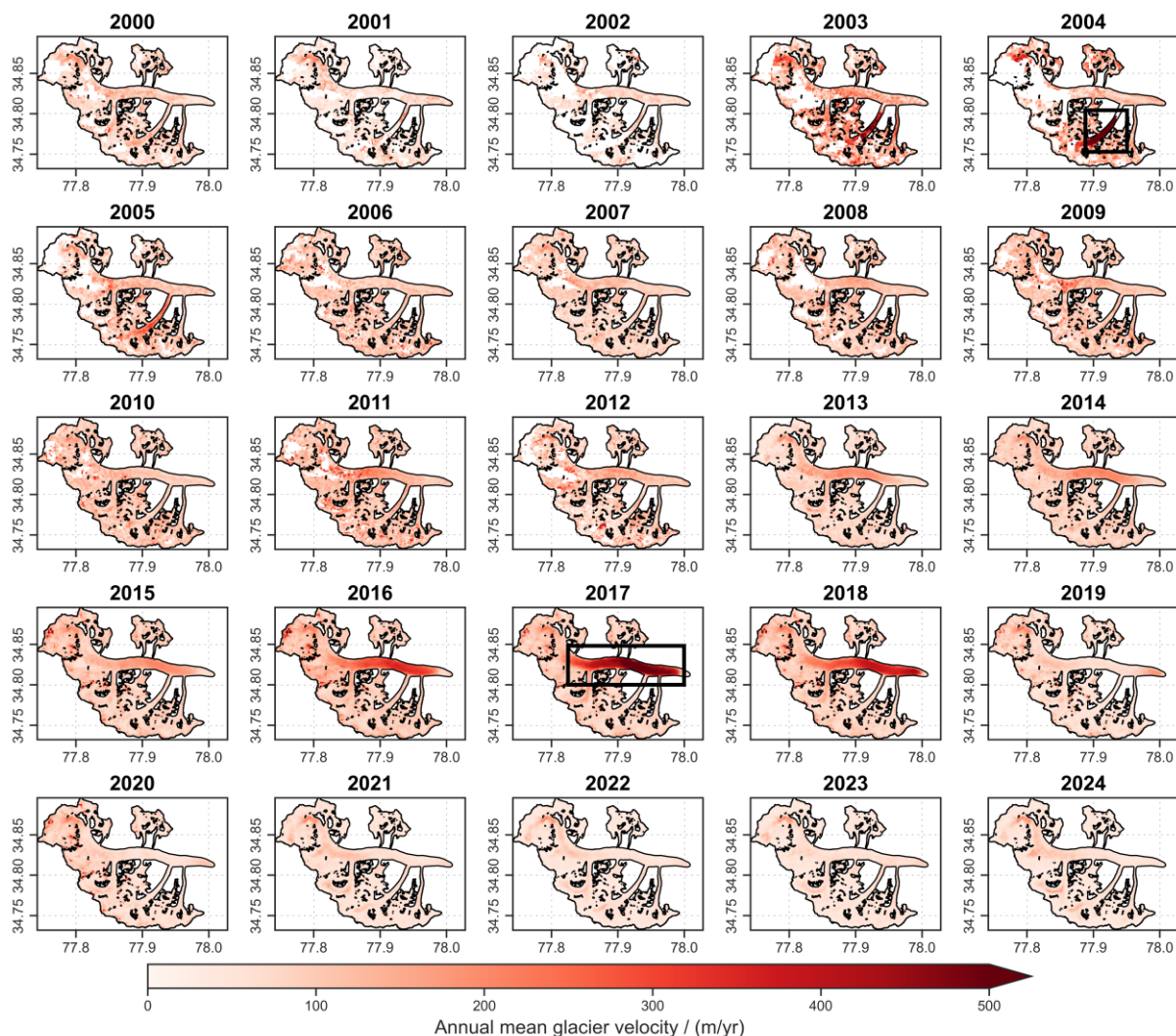


Figure 4: Annual mean velocities of NKG I from 2000 to 2024. Darker colors indicate higher velocities. The two black rectangles highlight the extents of the identified glacier surges. Glacier outlines are derived from RGI 6.0, with NKG V manually connected to NKG I.

295 To refine the timing of these surges, we calculated monthly mean velocity for the entire glacier as well as for key regions (Fig. 5). Regions B and C correspond to areas exhibiting the highest velocities during the second and first surges, respectively, and were used to investigate the temporal characteristics of these surge events. The glacier-wide mean velocity exhibited two distinct peaks in 2004 and 2017, aligning with the surges of NKG V and the main trunk, respectively. In Region B, glacier flow velocities remained relatively stable before June 2010, after which acceleration commenced. A
 300 notable increase was observed in June 2015, marking the onset of the surge. During the surge phase, three distinct acceleration and deceleration events occurred, with peak velocity reaching 757.9 m/yr in July 2017. Additional peaks were



recorded in November 2017 and July 2018. Following July 2018, glacier velocity declined sharply until September 2018, eventually stabilizing by June 2019. This suggests that the surge persisted for approximately four years, from June 2015 to June 2019. High-altitude velocity dynamics also confirm that, despite brief periods of increased flow exceeding 300 m/yr in 2011 and 2014, the surge of the main trunk began in June 2015. Region A, located downstream of Region B, exhibited a similar velocity pattern but with a delayed acceleration in June 2012.

In Region C, which was primarily affected during the first surge, velocity increases were first observed in November 2002, followed by rapid acceleration in November 2003. The surge peaked at 1,358.4 m/yr by September 2004 before rapidly declining, with velocities returning to normal by April 2005. This indicates a surge duration of approximately 2.5 years (November 2002–April 2005). However, data gaps between 2002 and 2005 introduce some uncertainty in precisely constraining the surge timing.

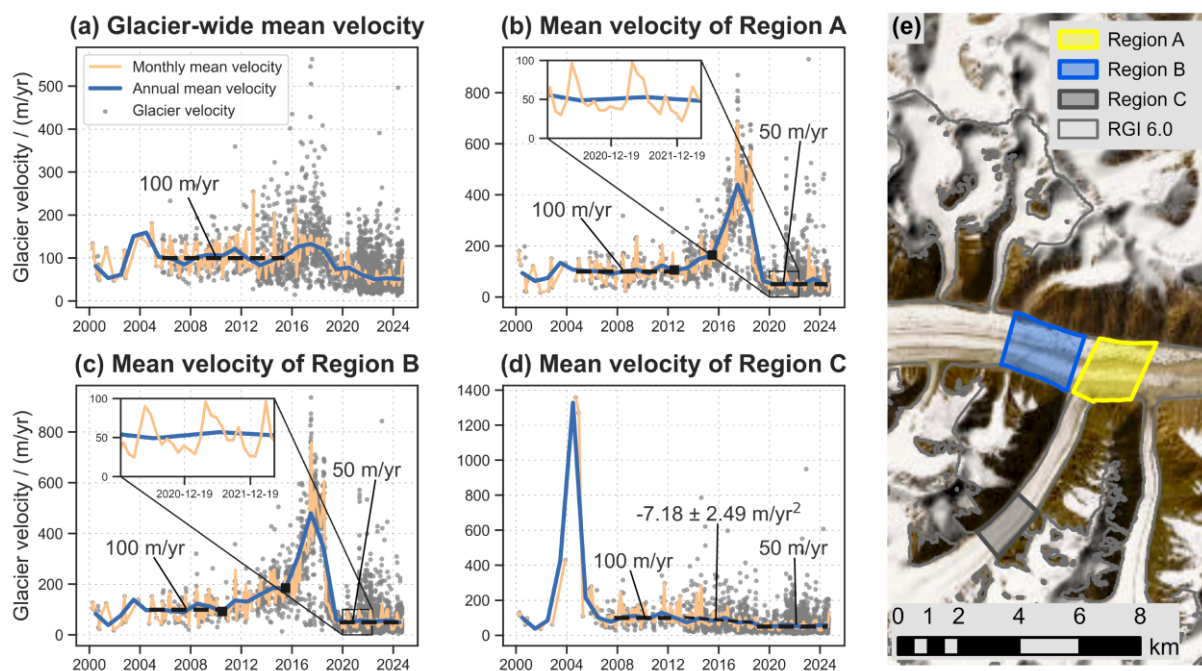


Figure 5: Glacier velocity time series for NKG I and Regions A, B, and C. The green line represents monthly mean glacier velocity, while the blue line denotes annual mean velocity. Each gray dot corresponds to an individual velocity observation. Panel (e) shows the locations of Regions A, B, and C. The basemap in panel (e) is derived from ESRI World Imagery and Hillshade (Credit: Esri, NASA, NGA, USGS, Earthstar Geographics, Sources: Esri, TomTom, Garmin, FAO, NOAA, USGS, © OpenStreetMap contributors, and the GIS User Community).

A comparative analysis of the two surges revealed distinctive post-surge behaviour patterns. Following the surge, the main trunk of NKG I exhibited a significant reduction in flow velocity, decreasing from a pre-surge stable-phase velocity of approximately 100 m/yr to around 50 m/yr post-surge. In contrast, NKG V initially returned to pre-surge velocities after its



surge but subsequently began a steady decline at a rate of 7.2 m/yr^2 from 2012 onward. This pattern aligns with the deceleration trends observed in other HMA glaciers (Dehecq et al., 2019), eventually stabilizing at approximately 50 m/yr in 2019. Notably, both NKG V (in 2001) and the main trunk (in 2010) exhibited pronounced deceleration phases before their respective surges, potentially indicating substantial internal dynamic shifts preceding surge initiation. Our analysis also identified clear intra-annual velocity variations (Fig. 5b and c). Under normal conditions (e.g., 2020), glacier velocity follows a seasonal pattern, peaking in May and June, followed by continuous deceleration until renewed acceleration begins in January of the following year. Additionally, a secondary velocity peak in September–October is evident, possibly linked to seasonal variations in glacier meltwater storage and drainage (Truffer et al., 2021).

4.2 Glacier surface elevation evolution

By integrating multisource remote sensing datasets, including Jason-3 (2016–2020), ICESat-2 (2019–2024), ASTER DEMs (2000–2019), and GF-7 DEM from July 2024, we reconstructed a time series of glacier surface elevation changes for NKG I. This analysis allowed us to capture distinct elevation variations across different glacier regions. Region A (Fig. 6a) exhibited the most complex elevation change patterns, characterized by six to seven distinct phases. Initially, from 2000 to September 2006, the surface elevation declined at a rate of 2.3 m/yr . This was followed by a four-year period of relative stability. Beginning in July 2010, the region experienced rapid elevation gain at a rate of 7.7 m/yr , though this increase was slightly slower before 2013. Between October 2018 and April 2020, surface elevation remained stable, after which it declined sharply over the following three years. In October 2023, a new phase of elevation increase commenced. Upstream Region B (Fig. 6b), the elevation trends were comparatively simpler. Initially, surface elevation decreased at a rate of 1.4 m/yr until January 2007. This was followed by a period of rapid elevation increase at 4.5 m/yr until May 2014, after which the growth rate moderated to 1.5 m/yr . In contrast, the upstream reservoir area exhibited an opposite trend, with gradual elevation increase at 0.2 m/yr before 2010, followed by a significant decline of 3.7 m/yr from 2010 to 2019.

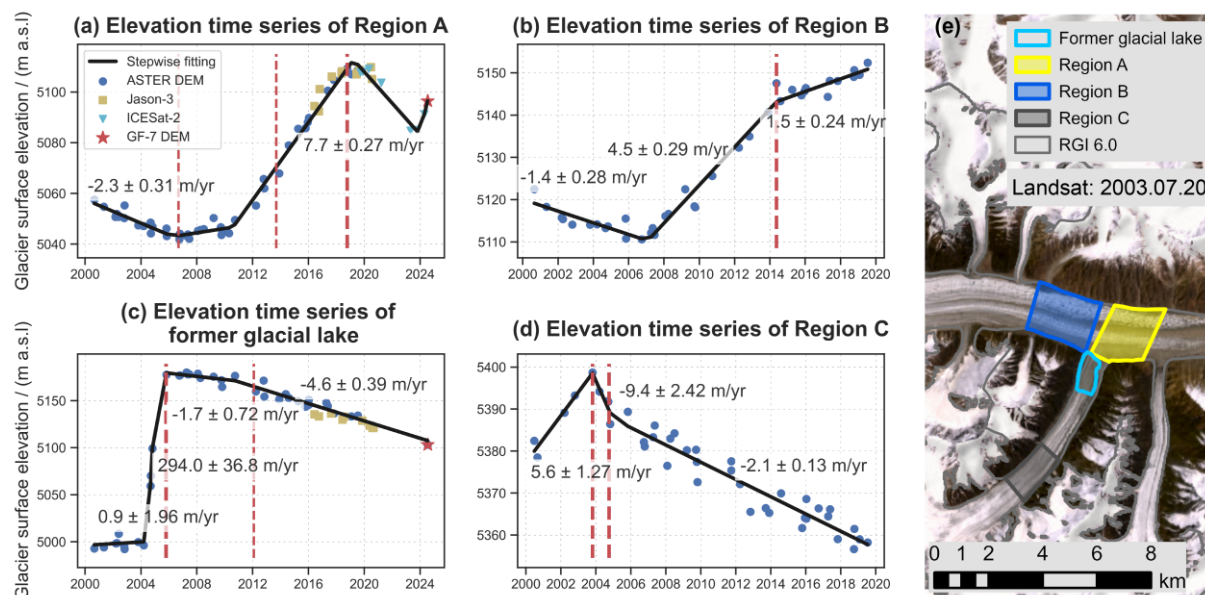


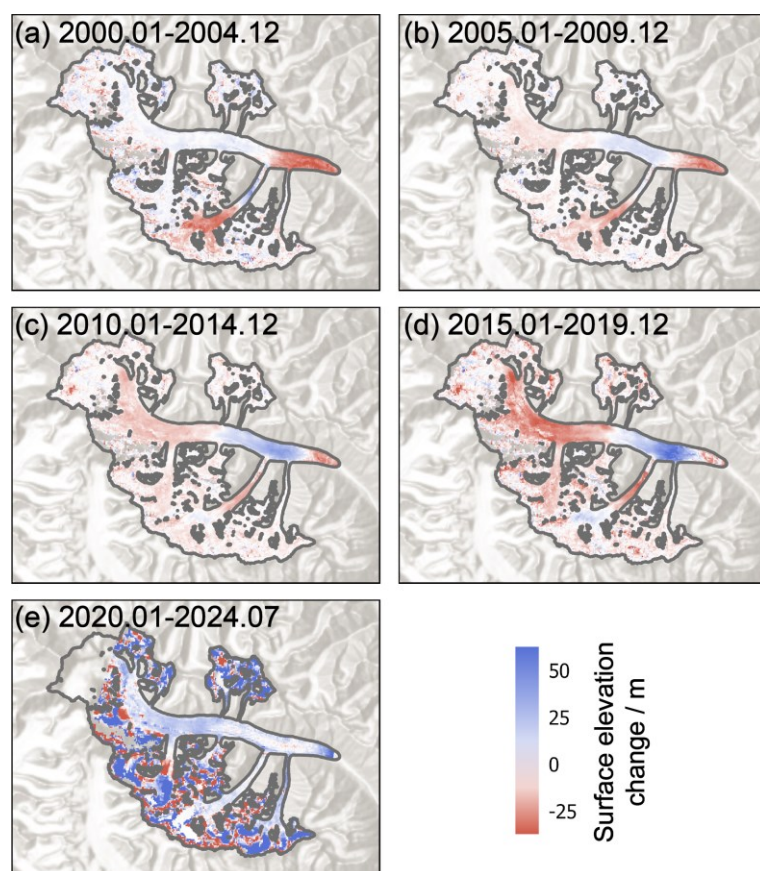
Figure 6: Glacier surface elevation time series of Regions A, B, C, and the former glacial lake from 2000 to 2024. (a)–(d) Black lines indicate elevation change trends, with each dot representing an individual elevation observation. Vertical red lines mark transition points in elevation change patterns. (e) Locations of Regions A, B, C, and the former glacial lake. The basemap in panel (e) is a Landsat 7 image acquired on July 20, 2003.

The former glacial lake, which was destroyed by the NKG V surge, displayed a distinct sequence of changes (Fig. 6c). Before 2004, the lake level rose gradually at a rate of 0.9 m/yr mainly due to glacier advance. However, following the substantial mass transfer during the surge, the main trunk’s obstruction led to an extreme increase in surface elevation in this region, with rates approaching 300 m/yr, peaking in October 2005. Over the subsequent five years, the surface elevation declined steadily at a rate of 1.7 m/yr. A sharp acceleration in surface lowering began in early 2012, reaching 4.6 m/yr, corresponding with the observed deceleration in glacier flow velocity in Region C (see Section 4.5). Region C exhibited a distinct pattern of elevation changes (Fig. 6d). It experienced rapid elevation gain until October 2003, followed by an abrupt decline lasting one year. The rate of decline moderated significantly after October 2004.

A spatial analysis of glacier elevation changes over the past 25 years, segmented into five-year intervals, revealed distinct temporal and spatial patterns of glacier evolution (Fig. 7). During the first five-year period (2000–2005), the surge of NKG V led to significant elevation loss in its high-altitude regions, while middle- and lower-altitude regions experienced elevation gains due to mass redistribution. Meanwhile, the main trunk of NKG I followed regular glacier behavior, with Region A and downstream areas undergoing surface lowering due to ablation, while upstream regions remained stable or experienced minor elevation increases.



Over the subsequent decade (2005–2015), the impact of the NKG V surge progressively propagated toward lower elevations. The areas that initially experienced elevation loss in the main trunk saw progressive downslope compression due to glacier movement, while subtle elevation decreases appeared in the upper regions. During the fourth five-year period (2015–2020), the main trunk surge caused substantial elevation reductions across extensive high-altitude regions. Concurrently, Region A experienced significant elevation gains, while the extent of elevation loss near the terminus further shrank. In the most recent five-year period (2020–2024), accumulated glacier mass in Region A migrated downstream toward the terminus, while glacier surface elevations in high-altitude regions increased rapidly. By this time, the influence of the NKG V surge on its surface elevation had largely dissipated.



370 **Figure 7: Glacier elevation change maps of NKG I over different time periods.** Blue areas indicate elevation gain, while red areas indicate elevation loss. (e) Uncertainties in high-altitude regions may arise due to snow cover. The basemaps in panels (a)–(e) are derived from ESRI World Hillshade (Credits: Esri, CGIAR, USGS).

4.3 Glacier extent and terminus position change

Glacier surges typically results in significant terminus advances. Using Sentinel-1 SLC images, we analysed the extent and terminus position changes of NKG I over the past decade. Annual terminus positions were averaged from measurements



taking in August, September, and October (Fig. 8a). Prior to 2018, the glacier experienced a minor retreat of approximately 40.3 m. This was followed by a rapid advance of 180.3 m between 2018 and 2022, after which the advance rate slowed down. Surface elevation changes at the terminus (Fig. 8c) exhibits a clear correlation with terminus position changes. Between 2000 and October 2018, the terminus elevation declined steadily at a rate of 3.3 ± 0.10 m/yr. This trend reversed between 380 October 2018 and December 2021, with an accelerated elevation gain of 14.1 ± 2.15 m/yr. Post-2022, while elevation continued to increase, the rate slowed to 6.0 ± 0.70 m/yr.

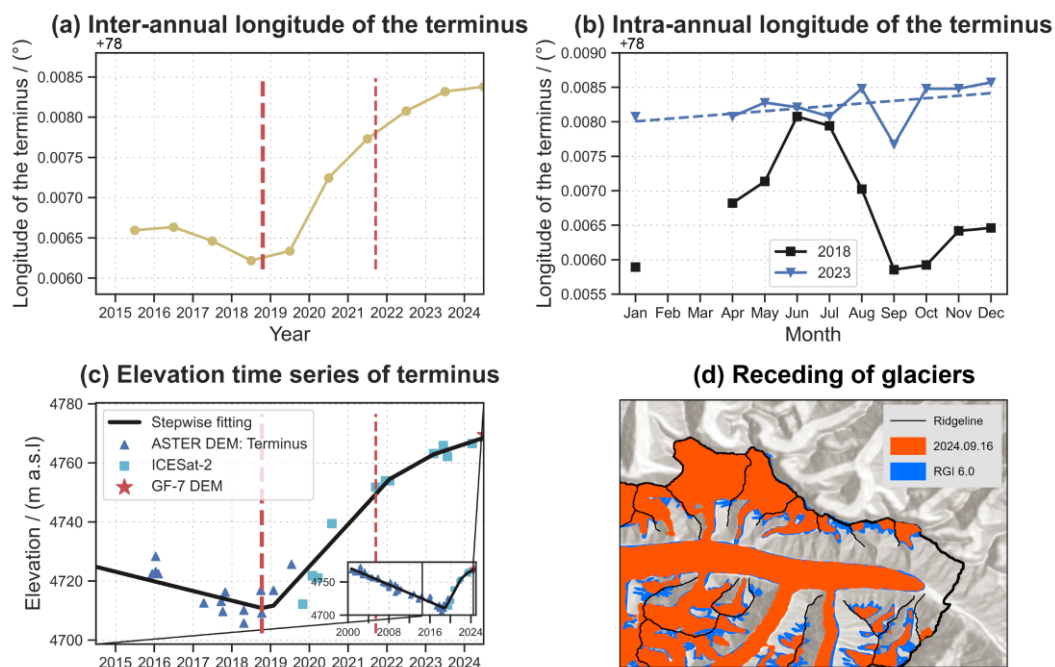


Figure 8: Terminus position and surface elevation changes over time. (a) Inter-annual terminus position changes derived from Sentinel-1 imagery; (b) Intra-annual terminus position variations derived from Sentinel-1 imagery; (c) Surface elevation time series at the glacier terminus, with the lower right subfigure displaying elevation changes from 2000 to 2024; (d) Glacier recession of NKG I, where blue represents the glacier extent derived from the RGI 6.0 inventory (August 2, 2002) and red depicts its configuration as of September 16, 2024. A longitude shift of 0.0005° in (a) and (b) corresponds to approximately 48.5 m in terminus position change. The basemap in panel (d) is derived from ESRI World Hillshade (Credit: Esri, NASA, NGA, USGS).

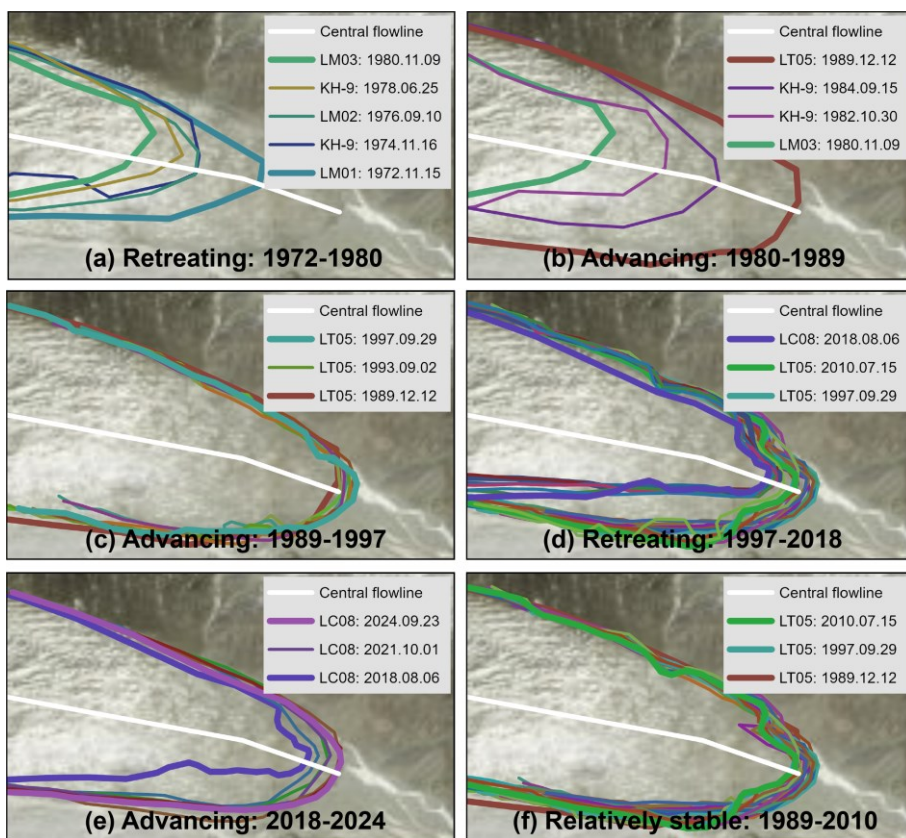
The high temporal resolution of Sentinel-1 data enabled a detailed analysis of intra-annual terminus variations (Fig. 8b). In 390 2018, before the main trunk surge reached the terminus, seasonal oscillations were evident: the terminus advanced to its farthest extent in June–July, retreated until September–October, and then resumed advancing in November. This pattern coincided with intra-annual velocity fluctuations. Initial calculations suggested an annual terminus displacement of 215.5 m in 2018, but comparison with Sentinel-2 (July 14, 2018) and Landsat 8 (October 25, 2018) images indicated a more modest change of 50 m. Overestimation in Sentinel-1-derived positions was likely influenced by the gray band (crevasse) near



395 longitude 78.0055° and seasonal snow cover in June and July. In contrast, year 2023 displayed a continuous advance throughout the year, culminating in a ~ 57 m net advance. The stark differences in intra-annual terminus behaviours between 2018 and 2023 highlight the pronounced impact of glacier surging on seasonal terminus fluctuations.

Over the past two decades, glacier extent has undergone notable changes (Fig. 8d). While the main trunk and terminus remained relatively stable, significant retreat occurred in the permanent snow cover at higher elevations and in peripheral glaciers within the basin, suggesting substantial glacier mass loss due to rising temperatures. With mass redistribution to lower elevations, NKG I is likely to experience greater mass loss in the coming years.

To mitigate potential biases in Sentinel-1-derived terminus positions caused by slow movement and seasonal snow cover, we manually delineated terminus positions using historical Landsat and KH-9 images from 1972 onward (Fig. 9), indicating two surges of the main trunk. The glacier retreated by approximately 600 m between 1972 and 1980, followed by an 1,100 m advance over 18 years (1980–1997). The second retreat (1997–2018) was more modest at 254 m. Post-2018, the terminus began advancing again, gaining 162 m and nearly returning to its 2000 position. Comparisons suggest that the 1980 surge was of greater magnitude than the 2017 surge. Notably, between 1989 and 2010, the terminus remained remarkably stable (Fig. 9f), with minimal changes in both position and morphology (Fig. 9f).





410 **Figure 9: Temporal evolution of the NKG I terminus position from 1972 to 2024.** (a) Terminus retreat from 1972 to 1980; (b) Rapid terminus advance between 1980 and 1989; (c) Slow terminus advance from 1989 to 1997; (d) Terminus retreat from 1997 to 2018; (e) Terminus advance from 2018 to 2024; and (f) Period of relative terminus stability between 1989 and 2010. Colored lines represent terminus positions and morphological changes at different time steps. The basemaps in panels (a)–(f) are derived from ESRI World Imagery and Hillshade (Credits: Esri, NASA, NGA, USGS, Maxar).

415 4.4 Surge-induced glacial lake evolution

During our analysis of Jason-3 data, we identified the formation of a small ice-dammed lake, triggered by the glacier flow of the main trunk. Prior to 2012, the tributary glacier (Point B) maintained a slightly higher surface elevation than the main trunk, allowing for natural drainage of meltwater and precipitation (Fig. 10a). However, after 2012, the surface elevation of the main trunk (Point A) progressively exceeded that of the tributary glacier. This elevation disparity was further exacerbated
420 by the 2017 surge of the main trunk, which altered the local topography and obstructed meltwater drainage from both the tributary glacier and NKG V, ultimately leading to lake formation.

Jason-3 observations captured a sudden drop in lake level during the summer of 2018, a phenomenon corroborated by ASTER DEM time series, which documented a similar rapid decline in summer 2019. To further investigate these events, we utilized high-resolution Sentinel-1 and Sentinel-2 images to delineate lake boundaries between July and October 2018 (Fig.
425 10c-h). The lake remained relatively stable at approximately 0.11 km² from July to early August before expanding rapidly to 0.145 km² by late August, coinciding with peak water levels. During this period, floating ice masses migrated northeastward, indicating that the discharge process has commenced. By mid-September, the lake experienced a rapid reduction in area, with no subsequent recovery observed through mid-October. Analysis of the C-C' elevation profile (Fig. 10b) suggests that a drainage event occurred in early September, consistent with the findings of Lovell and Muhammad (2024). A similar
430 drainage event likely explains the abrupt water level reduction observed in 2019.

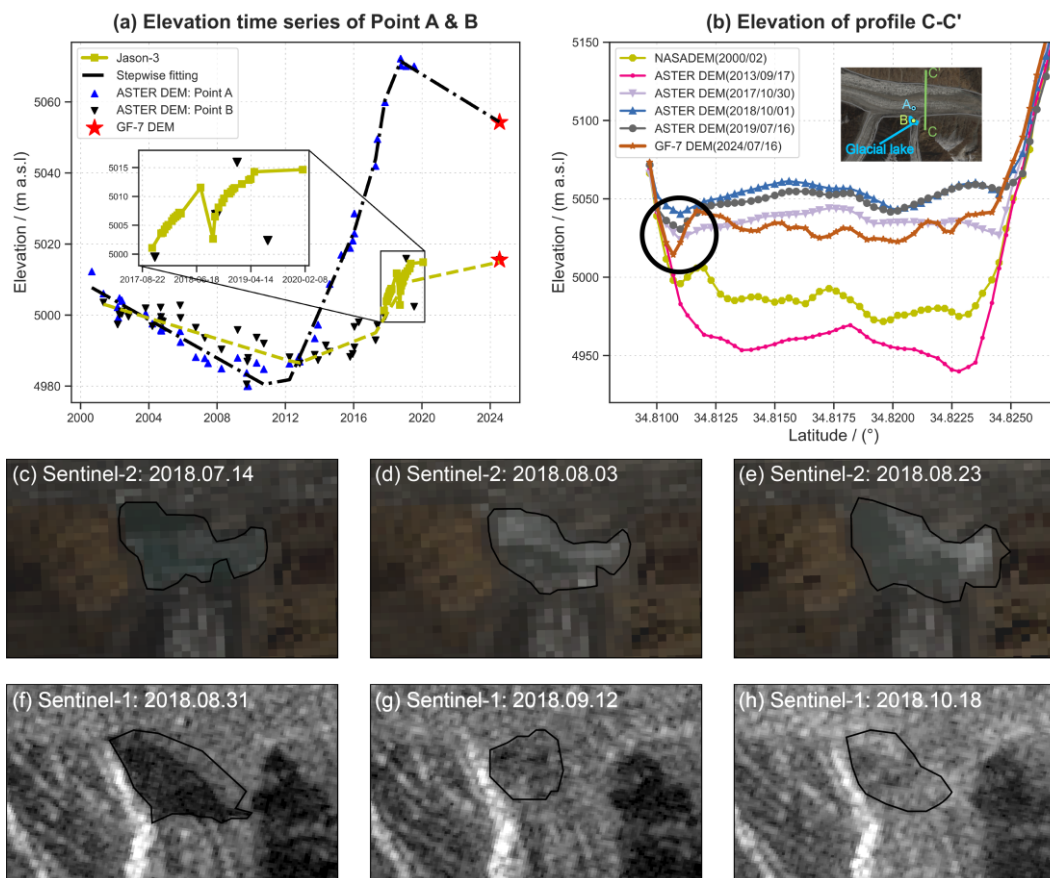


Figure 10: Evolution of the glacial lake. (a) Surface elevation time series at Points A and B. The inset highlights lake level variations observed by Jason-3. (b) Elevation profile along cross-section C-C' at different time periods. (c)–(e) Glacial lake extents derived from Sentinel-2 images. (f)–(h) Glacial lake extents retrieved from Sentinel-1 GRD images. Basemap of the insert map in panel (b) is a Sentinel-2 image acquired on August 23, 2018.

435

Analysis of the July 2024 GF-7 DEM revealed that the glacial lake maintained a water level of approximately 5,015 m during the summer of 2024, comparable to peak levels recorded in 2018 and 2019. These observations indicate that the lake functions as a small, seasonally cyclic glacial lake system, characterized by water accumulation during autumn through spring, followed by discharge events in the summer. Additionally, observations from July 2024 indicate that the surface elevation of the main trunk at Point A has decreased relative to 2019, with an elevation change rate of -3.0 m/yr, closely approximating the pre-2012 rate of -2.9 m/yr. Given the current elevation patterns, the persistence of this glacial lake in coming years appears likely. Furthermore, the GF-7 DEM cross-section (black circle in Fig. 10b) revealed a deep trough adjacent to the ice-dammed lake, with a minimum elevation of approximately 5,014.4 m, nearly equivalent to contemporary peak lake levels. This topographic configuration suggests that any further rise in lake level could potentially trigger future discharge events or overflow conditions.

445



Analysis of historical KH-9 and Landsat 2 imagery provides additional context for the region's glacial lake evolution. The former proglacial lake fronting NKG V emerged around 1978 and persisted for an extended period. The June 1978 KH-9 image indicates that its formation resulted from a rise in the main trunk elevation, which impeded meltwater drainage, a mechanism analogous to that observed in the tributary glacier. As the NKG V terminus underwent sustained meltwater inundation and progressive ablation, the lake expanded to 0.61 km² by August 1991 and remained at approximately 0.6 km² throughout the following decade. However, the surge of NKG V led to the complete disappearance of this glacial lake by the end of 2004, with accumulated meltwater releasing gradually over the course of less than a year.

4.5 Spatiotemporal correlation among different characteristics

In Sections 4.1–4.4, we examined the flow velocity, surface elevation, terminus position, and glacial lake evolution of NKG I using multisource remote sensing data, including altimetry footprints and optical and SAR images. However, these characteristics are not independent but rather interdependent, reflecting the dynamic nature of glacier systems. Here we analyse spatiotemporal correlations among four key surge parameters, i.e., flow velocity in Region B, surface elevation changes in Region A, terminus position variations, and the evolution of the tributary glacial lake, through a chronological assessment (Fig. 11).

Surge-type glaciers typically undergo prolonged quiescent phases interrupted by short-lived surges. The main trunk of NKG I remained in a quiescent phase for approximately 35 years before its surge initiated in 2015. Before 2010, flow velocity in Region B remained relatively stable, while surface elevation in Region A initially decreased before stabilizing with minor increases after 2006. The glacier terminus showed little positional change during this period. Between 2010 and 2015, Region B exhibited progressive velocity acceleration, coinciding with significant surface elevation gains in Region A. Meanwhile, terminus retreat persisted. The surge phase initiated in 2015, marked by a rapid increase in velocity in Region B, which peaked in 2017, along with accelerated surface elevation gains in Region A and continued terminus retreat. From 2017 to 2019, velocity in Region B declined rapidly, while surface elevation in Region A continued to rise for an additional year before stabilization. Terminus advance began after 2018. Between 2019 and 2024, flow velocity in Region B decreased to lower than pre-surge levels and remained stable, signalling the transition into a new quiescent phase. Surface elevation in Region A exhibited three distinct stages: stability, decline, and subsequent increase, while the terminus continued to advance. Notably, the time lag between changes in flow velocity in Region B, surface elevation in Region A, and terminus position variations progressively increased over time, reflecting the downstream propagation of surge effects.

In contrast to the surface elevation and terminus position, the formation of the glacial lake was primarily driven by the surface elevation of the main trunk exceeding the terminus elevation of the tributary glacier, obstructing meltwater drainage. The subsequent surge of the main trunk further amplified this elevation difference, leading to a rise in lake water level. However, cracks that developed due to rapid movement during the surge prevented further accumulation, causing the lake to drain once its level exceeded a critical threshold. This resulted in periodic fluctuations in lake water levels.

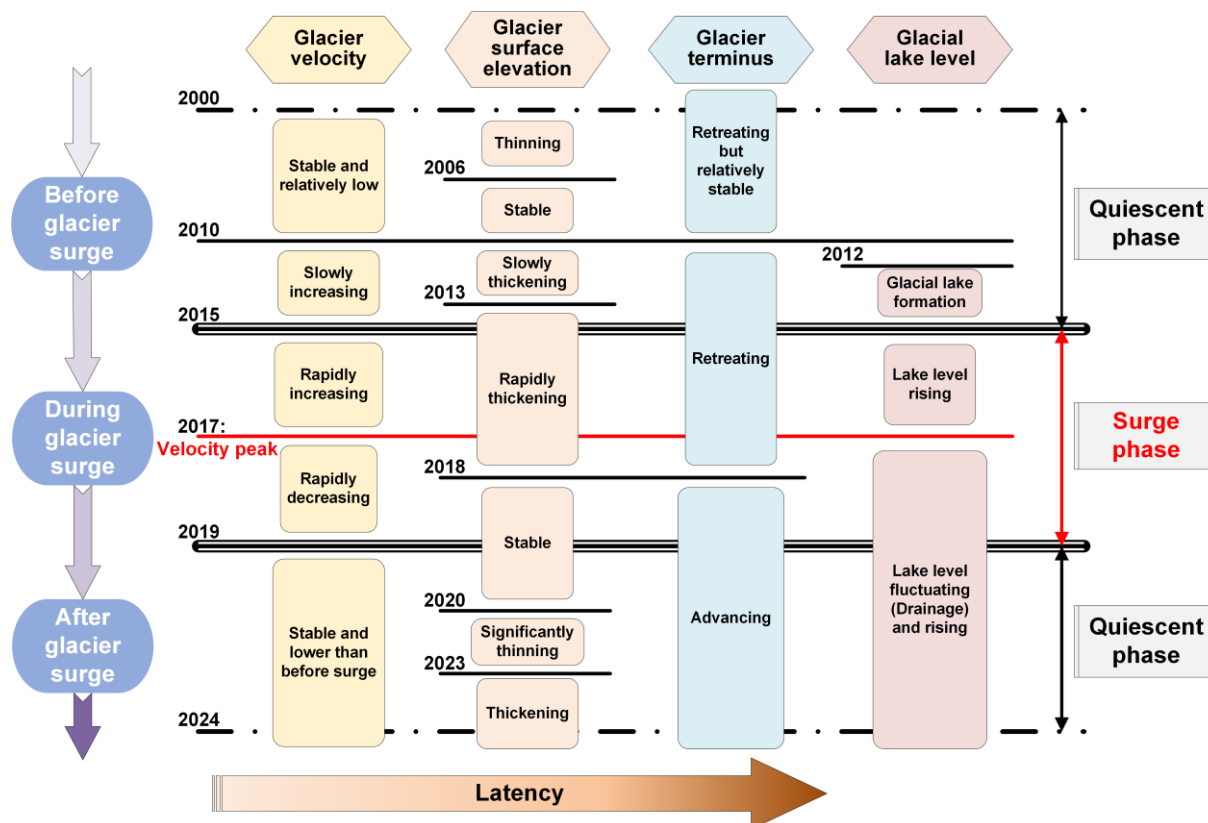


Figure 11: Spatiotemporal correlations among glacier flow velocity, surface elevation, and terminus position during different surge

480 **stages.** The left and right columns represent different phases of the glacier surge. Coloured boxes correspond to specific phase of different variables, with the associated year indicated in the upper left corner of each horizontal line. Arrows at the bottom illustrate the latency in the propagation of surge effects, with redder tones denoting longer delays.

485 Given the strong interdependencies among these variables, it is possible to estimate one variable based on observations of another. For instance, mean velocity over a specific period can be inferred from spatial changes in glacier elevation, similar to velocity retrieval using optical or SAR image correlation techniques. Conversely, rapid velocity variations can provide insight into elevation change trends. Due to uneven velocity distributions across the glacier, a rapid velocity increase in one location often leads to an elevation increase in downstream regions with slower movement. Conversely, when glacier velocity decreases, surface elevation in downstream areas either declines or exhibits a slower rate of increase. Additionally, a rapid velocity increase near the terminus typically signals terminus advance, whereas stabilization of surface elevation following a period of decline suggests terminus retreat.

490



5. Discussion

5.1 Potential of Jason-3 and multisource remote sensing in monitoring mountain glaciers and glacial lakes

Originally designed for monitoring global sea levels, wave heights, and ocean surface wind speeds, Jason-3 has increasingly been applied to inland water bodies, rivers, and ice sheet elevations (Crétaux et al., 2018; Huang et al., 2018; Biancamaria et al., 2018; Biancamaria et al., 2017). However, its application in mountain glacier research remains limited (Hwang et al., 2021). Our study demonstrates that, with appropriate waveform retracking, waveform selection, and observation point filtering, Jason-3 is capable of effectively monitoring large glaciers and small glacial lakes in HMA. Despite its relatively low spatial resolution, Jason-3's high temporal resolution (10 days) and fixed ground tracks offer significant advantages. Under certain conditions, its observation frequency can even surpass that of satellites like ICESat-2.

In the case of NKG I, our analysis of 653 Jason-3 footprints from 2016 to 2020 identified 177 valid footprints for glacial lake monitoring and 96 for glacier surface elevation monitoring, yielding an overall validity rate of 42%. This demonstrates Jason-3's potential for capturing both glacier and glacial lake dynamics over time. Furthermore, by integrating historical data from TOPEX/Poseidon (T/P), Jason-1/2, and contemporary Jason-CS (Sentinel-6) with Jason-3 observations (Tao et al., 2023), it is possible to achieve continuous, long-term monitoring spanning over 30 years in suitable regions (Schröder et al., 2019).

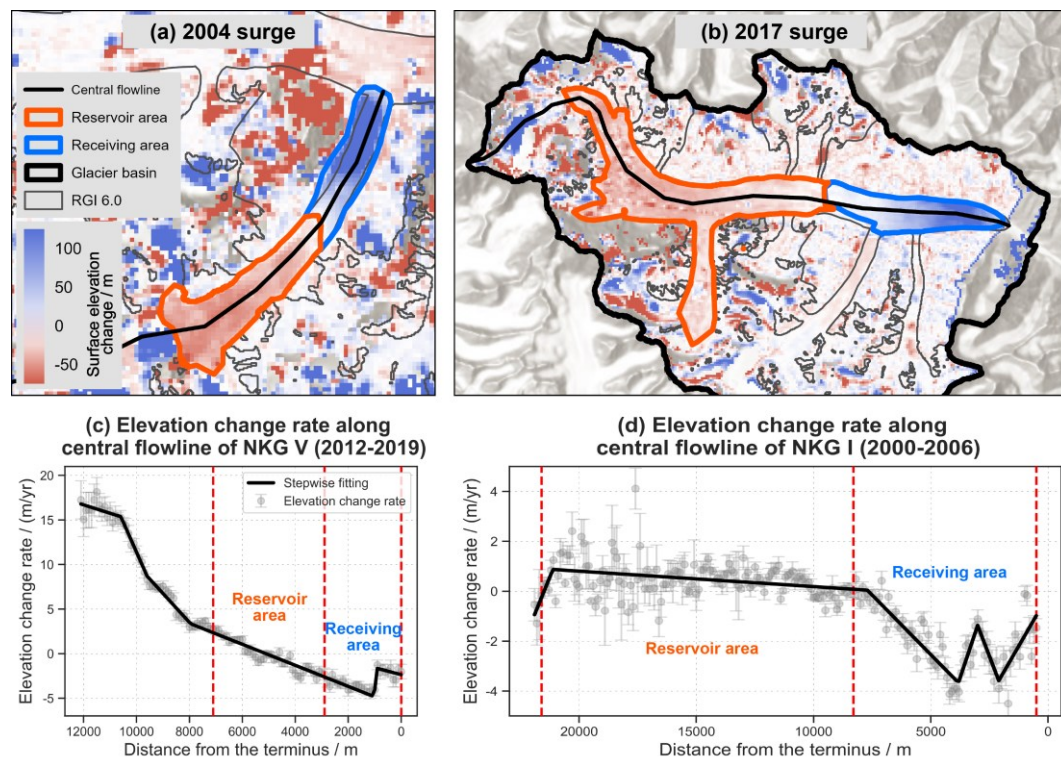
Beyond the T/P-Jason series, incorporating data from DEMs (e.g., ASTER DEM and TerraSAR/TanDEM DEM (Wu et al., 2018)), and other altimetry satellites (e.g., ICESat-2, GEDI, SWOT, Sentinel-3, CryoSat-2, and ICESat) further enhances observation frequency and spatial coverage. This multisource approach enables the effective monitoring of short-term events such as glacial lake outburst floods and ice avalanches while also facilitating cross-validation with data from different sensors, thereby improving the accuracy and reliability of measurements. For glacier surges that unfold over several years, this approach can aid in detecting early-stage surface activity (Jiang et al., 2021), predicting surge propagation dynamics, and assessing potential downstream impacts—critical insights for disaster prevention and risk mitigation. These capabilities are particularly valuable in data-scarce and logistically challenging regions like HMA, where in-situ measurements are often limited. Additionally, in areas with extensive ground-based observations, this approach serves as an important independent validation tool, complementing existing datasets and improving overall monitoring accuracy.

5.2 Surge-induced glacier mass transfer

To assess mass transfer during the two glacier surges, we selected high-quality ASTER DEMs captured before and after each event. The pre-surge DEM for NKG V was acquired on October 21, 2002, and the post-surge DEM on October 16, 2006. For the main trunk of NKG I, the pre-surge DEM was obtained on October 16, 2015, while the post-surge DEM was from July 16, 2019. By analysing elevation changes between these periods, we manually delineated the reservoir and receiving areas of the surges (Fig. 12a and b). However, given the presence of data gaps and errors in the DEMs, particularly in high-altitude



regions (Paul et al., 2017), the delineated reservoir areas may deviate from actual reservoir extents. As a result, our estimation of mass transfer primarily relies on the receiving areas, where elevation change signals are more clearly captured.



525 **Figure 12: Glacier elevation changes during surges and elevation change rates along central flowlines during stable periods.** (a) Elevation changes of NKG V between 2002 and 2006; (b) Elevation changes of NKG I between 2015 and 2019; (c) Elevation change rates along the central flowline of NKG V during the period (2012–2019); (d) Elevation change rates along the central flowline of NKG I during the period (2000–2006). The areas between the vertical dashed lines in (c) and (d) correspond to the reservoir and receiving areas shown in (a) and (b). The basemap in panel (b) is derived from ESRI World Hillshade (Credit: Esri, NASA, NGA, USGS).

530 During the 2004 surge of NKG V (November 2002–April 2005), the volume of ice transported downstream was estimated at 0.24 km³. Similarly, the 2017 surge of the main trunk (June 2015–June 2019) resulted in a larger volume transfer of 0.46 km³ (Table 2). However, glacier surges are accompanied not only by mass transport but also other concurrent accumulation and ablation processes. To account for these, we extracted and fitted the elevation change rates during stable periods along the central flowlines (i.e., 2012–2019 for NKG V and 2000–2006 for the main trunk), and used these rates to approximate the elevation change patterns attributed to precipitation and melting during the surges (Fig. 12c and d). Given the relatively

535 elevation change patterns attributed to precipitation and melting during the surges (Fig. 12c and d). Given the relatively minor temperature fluctuations in the NKG region between 2000 and 2019, the uncertainties in our ablation estimates remain within acceptable limits. After these corrections, the glacier volume change in the receiving areas was revised upward by 14.9% for NKG V and 15.6% for the main trunk.



By converting glacier volume into mass using a mean glacier density of $850 \pm 60 \text{ kg/m}^3$ (Huss, 2013) and propagating errors accordingly, we estimated that the 2004 surge of NKG V transferred a total mass of $0.23 \pm 0.02 \text{ Gt}$, while the 2017 surge of the main trunk transferred $0.45 \pm 0.03 \text{ Gt}$ (Table 2). The impacts of these mass transfers, however, differed significantly. In the case of NKG V, the main trunk acted as a barrier, preventing substantial mass transport beyond the former glacial lake site. Consequently, the surge's influence on the entire NKG I system remained relatively limited. In contrast, the main trunk's surge resulted in a more extensive and impactful mass redistribution.

Table 2 Glacier mass transfer during glacier surges.

Surge	Region	Volume change / (10^6 m^3)	Elevation change rate / (m/yr)	Volume correction / (10^6 m^3)	Volume change after correction/ (10^6 m^3)	Mass change after correction/ (Gt)
2004 surge	Receiving area	237.62 ± 9.96	-3.04 ± 0.107	-35.38 ± 3.75	273.00 ± 10.65	0.232 ± 0.017
	Reservoir area	-83.53 ± 7.97	-0.20 ± 0.059	-3.95 ± 1.21	-79.57 ± 8.06	-0.067 ± 0.008
2017 surge	Receiving area	461.49 ± 11.13	-1.90 ± 0.044	-71.85 ± 7.37	533.34 ± 13.35	0.453 ± 0.030
	Reservoir area	-441.09 ± 5.38	0.47 ± 0.044	53.74 ± 7.37	-494.83 ± 9.12	-0.421 ± 0.028

With a considerable volume of ice now reaching the terminus and regional temperatures continuing to rise (Fig. 13a), we anticipate a significant increase in glacier runoff in the coming years. This could heighten flood risks, particularly during the summer months when glacier discharge is at its peak. Additionally, we observed a rapid rise in surface elevation in the high-altitude regions of NKG V after 2012 (Fig. 12c), suggesting that the firm basin is still accumulating mass and that the glacier remains in a quiescent phase. In contrast, the surface elevation changes in the high-altitude areas of the main trunk between 2000 and 2006 were minimal (Fig. 12d), indicating substantial ice accumulation in the reservoir area. If this accumulation continues to exceed the critical threshold, it could potentially trigger another glacier surge, as observed when the main trunk entered its surge phase in 2015.

5.3 Response of glacier surge and movement to climate change

We analysed long-term changes in temperature, precipitation, snowfall, snow albedo, net radiation, and net solar radiation in the NKG region since 1950 using ERA5-Land Monthly Aggregated data (Fig. 13). Results indicate that between 1984 and 1999, increased snowfall contributed to substantial glacier mass accumulation in the region. During this period, both NKG V and the main trunk of NKG I experienced significant mass gain and increased driving stress. Additionally, elevated temperatures in 2015/2016, increased snowfall in 2015, and heightened net radiation from 2015 to 2017 likely played a crucial role in modifying the internal drainage system, enhancing glacier meltwater availability and accelerating glacier flow, thereby triggering the main trunk surge. Significantly higher net radiation in 2000/2001 also likely played a key role in



triggering the NKG V surge. These findings suggest that the mechanisms driving glacier surges in this region are consistent with those documented in other Karakorum glaciers (Jiang et al., 2021).

565 Notably, NKG V surged first, likely due to its steeper surface slope (4.75°) compared to the main trunk of NKG I (2.21°), as well as enhanced erosion caused by the former proglacial lake. Historical climate records indicate that from 1977 to 1980, temperatures in the NKG region were higher than average, and net radiation from 1970 to 1980 was significantly greater than in the previous decade. These factors might collectively trigger the 1980 surge. Furthermore, NKG I had undergone prolonged retreat, with its main trunk nearly 900 m shorter than that before the 2017 surge. As a result, after the 1980 main trunk surge, the glacier terminus rapidly advanced more than 1,000 m in nine years.

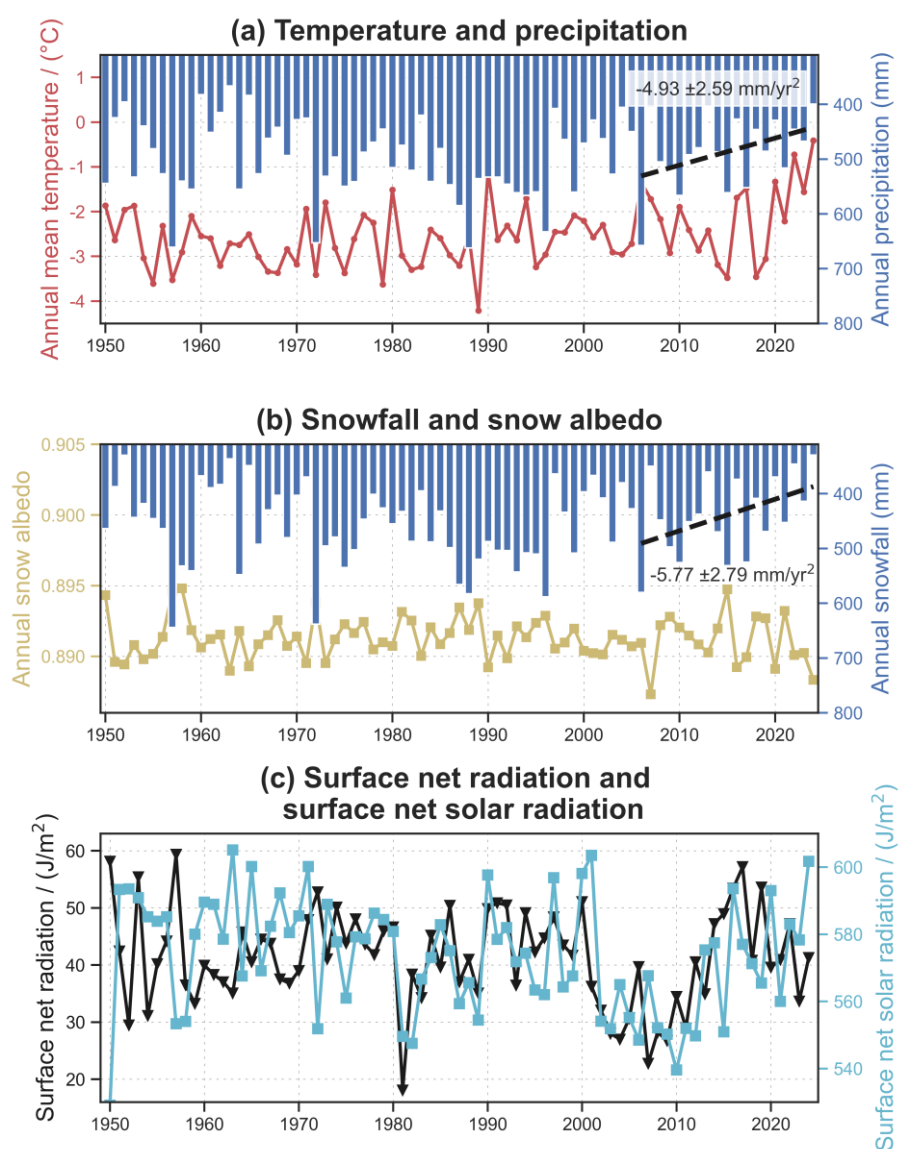




Figure 13: Changes in meteorological variables in the NKG region since 1950. (a) Temperature and precipitation, (b) Snowfall and snow albedo, and (c) Surface net radiation and surface net solar radiation. Lines of different colours represent different meteorological variables, each corresponding to its respective y-axis label. Bars in (a) and (b) denote annual total precipitation and snowfall, respectively.

A comparison of the two surges of the main trunk in 1980 and 2017 reveals distinct differences in terminus behaviour following each event. After the 1980 surge, the terminus continued to advance for nearly ten years before stabilization for almost two decades. In contrast, following the 2017 surge, rapid terminus advance lasted only about four years before slowing down. By late 2024, the terminus position showed minimal movement compared to 2023 (Fig. 9).

Several factors likely contributed to this difference. First, the main trunk was significantly shorter in 1980 than in 2017. Second, post-2019 warming, coupled with reduced precipitation and snowfall since 2010, played a crucial role in limiting post-surge terminus advance in recent years. As temperatures continue to rise and precipitation phases shift, future glacier surges in NKG I may increasingly be controlled by hydrological processes. This transition could lead to reduced surge magnitude, shorter return periods, and greater instability in glacier structure. Given the significant warming and climate extremes recently, the likelihood of glacier-related hazards may increase not only in NKG I but also across the Karakoram region and broader HMA (Kääb et al., 2018), with potential implications on a global scale. These findings highlight the growing need for improved glacier hazard monitoring, disaster prevention strategies, and mitigation efforts in response to evolving glacial dynamics in a warming climate.

6. Conclusion

Using multisource remote sensing data, we analysed the spatiotemporal evolution of glacier flow velocity, surface elevation, terminus position, and surge-induced glacial lake during two surge events of NKG I. Our results reveal distinct phases of glacier surge dynamics and their response to climate variability. Prior to both surges, the glacier flow velocity exhibited a notable deceleration compared to the quiescent-phase velocity (approximately 100 m/yr). Velocity then gradually increased until reaching a critical threshold and initiating the surge phase, which persisted for several years. During surging, while velocity fluctuated, it remained consistently elevated. Substantial glacier mass was transported to lower elevations, causing abrupt changes in surface elevation. For instance, the 2017 surge of the main trunk transferred nearly 0.45 ± 0.03 Gt of glacier mass to the receiving area, leading to an elevation increase of around 30 m in Region A. The 2004 surge of NKG V caused even more dramatic elevation changes, with an increase of 180 m in the former glacial lake within one year. Following this event, advancing tongue destroyed the proglacial lake that had persisted for nearly three decades.

During the late surge phase, flow velocity declined sharply to a lower level, marking the transition back to the quiescent phase. Following the sharp decline, the glacier further decelerated to velocities comparable to or even lower than pre-surge levels, until it stabilized. For instance, the main trunk's stable post-surge velocity was only half of its pre-surge value. Post-surge, surface elevation changes varied across different glacier sections. Additionally, the main trunk obstructed the



meltwater outlet of a tributary glacier and NKG V, leading to the formation of a small ice-dammed lake that underwent seasonal storage and drainage cycles.

605 Analysis of historical glacier terminus fluctuations revealed a surge event of the main trunk around 1980 that was larger in magnitude and exhibited a longer rapid advance period than the 2017 surge. Additionally, after the 2004 surge, NKG V began to decelerate after remaining stable flow velocities for nearly five years. These changes, along with our examination of meteorological variables, suggest that ongoing climate change may alter surge mechanisms, potentially reducing surge magnitudes while increasing surge frequency. However, further observations and case studies are required to confirm these trends.

610 This study enhances our understanding of glacier surges in NKG I and the Karakoram region, providing valuable insights into surge dynamics and their climate-driven triggers. The integration of multisource remote sensing datasets, including satellite altimetry, DEMs, optical imagery, and SAR observations, demonstrates the power of comprehensive remote sensing analyses for glacier studies. Our findings also contribute critical insights for future research on glacier surging mechanisms and offer validation data for numerical models of glacier surge behaviour.

615 **Code and data availability**

The data and code presented in this study are available on a reasonable request from the corresponding author.

Author contributions

DL conceived the project, conceptualized the paper, and developed the methodology. FZ developed the methodology, curated the data, made the figures, and prepared the original draft. DL, CF, YW, and XD reviewed and edited the paper.

620 **Competing interests**

The authors declare no conflict of interest.

Acknowledgments

625 We acknowledge the AVISO for providing Jason-3 SGDR-F data, the NSIDC for providing ICESat-2 L3A land ice height (ATL06) dataset, the ASF for providing Sentinel-1 SLC/GRD images and HyP3 service, the USGS and GEE for providing Landsat images, Sentinel-2 images, and KH-9 images, the JPL/NASA for providing the ITS_LIVE dataset and NASADEM, and OpenTopography for providing Copernicus DEM. We appreciate Dr. Hugonnet Romain from Civil and Environmental Engineering and the eScience institute at the University of Washington for providing their bias-corrected ASTER DEMs



spanning from 2000–2019. Reviewers and editors' comments that are useful in improving this study and manuscript are acknowledged.

630 **Financial support**

This study was supported by the National Natural Science Foundation of China (Grant No. 52325901).

References

- Aja-Fernández, S. and Alberola-López, C.: On the estimation of the coefficient of variation for anisotropic diffusion speckle filtering, *Ieee T Image Process*, 15, 2694-2701, <https://doi.org/10.1109/Tip.2006.877360>, 2006.
- 635 Barrant, N. E. and Murray, T.: Multivariate controls on the incidence of glacier surging in the Karakoram Himalaya, *Arct Antarct Alp Res*, 38, 489-498, [https://doi.org/10.1657/1523-0430\(2006\)38\[489:Mcotio\]2.0.Co;2](https://doi.org/10.1657/1523-0430(2006)38[489:Mcotio]2.0.Co;2), 2006.
- Bazai, N. A., Cui, P., Carling, P. A., Wang, H., Hassan, J., Liu, D. Z., Zhang, G. T., and Jin, W.: Increasing glacial lake outburst flood hazard in response to surge glaciers in the Karakoram, *Earth-Sci Rev*, 212, 103432, <https://doi.org/10.1016/j.earscirev.2020.103432>, 2021.
- 640 Berthier, E. and Brun, F.: Karakoram geodetic glacier mass balances between 2008 and 2016: persistence of the anomaly and influence of a large rock avalanche on Siachen Glacier, *J Glaciol*, 65, 494-507, <https://doi.org/10.1017/jog.2019.32>, 2019.
- Bhambri, R., Hewitt, K., Kawishwar, P., and Pratap, B.: Surge-type and surge-modified glaciers in the Karakoram, *Sci Rep-Uk*, 7, 15391, <https://doi.org/10.1038/s41598-017-15473-8>, 2017.
- Biancamaria, S., Frappart, F., Leleu, A. S., Marieu, V., Blumstein, D., Desjonquères, J. D., Boy, F., Sottolichio, A., and
645 Valle-Levinson, A.: Satellite radar altimetry water elevations performance over a 200 m wide river: Evaluation over the Garonne River, *Adv Space Res*, 59, 128-146, <https://doi.org/10.1016/j.asr.2016.10.008>, 2017.
- Biancamaria, S., Schaedele, T., Blumstein, D., Frappart, F., Boy, F., Desjonquères, J. D., Pottier, C., Blarel, F., and Niño, F.: Validation of Jason-3 tracking modes over French rivers, *Remote Sens Environ*, 209, 77-89, <https://doi.org/10.1016/j.rse.2018.02.037>, 2018.
- 650 Bolch, T., Kulkarni, A., Kääb, A., Huggel, C., Paul, F., Cogley, J. G., Frey, H., Kargel, J. S., Fujita, K., Scheel, M., Bajracharya, S., and Stoffel, M.: The State and Fate of Himalayan Glaciers, *Science*, 336, 310-314, <https://doi.org/10.1126/science.1215828>, 2012.
- Brun, F., Berthier, E., Wagnon, P., Kaab, A., and Treichler, D.: A spatially resolved estimate of High Mountain Asia glacier mass balances from 2000 to 2016, *Nat Geosci*, 10, 668-673, <https://doi.org/10.1038/Ngeo2999>, 2017.
- 655 Clarke, G. K. C., Collins, S. G., and Thompson, D. E.: Flow, Thermal Structure, and Subglacial Conditions of a Surge-Type Glacier, *Can J Earth Sci*, 21, 232-240, <https://doi.org/10.1139/e84-024>, 1984.



- Crétaux, J. F., Bergé-Nguyen, M., Calmant, S., Jamangulova, N., Satylkanov, R., Lyard, F., Perosanz, F., Verron, J., Montazem, A. S., Le Guilcher, G., Leroux, D., Barrie, J., Maisongrande, P., and Bonnefond, P.: Absolute Calibration or Validation of the Altimeters on the Sentinel-3A and the Jason-3 over Lake Issykkul (Kyrgyzstan), *Remote Sens-Basel*, 10, 1679, <https://doi.org/10.3390/rs10111679>, 2018.
- Crippen, R., Buckley, S., Agram, P., Belz, E., Gurrola, E., Hensley, S., Kobrick, M., Lavallo, M., Martin, J., Neumann, M., Nguyen, Q., Rosen, P., Shimada, J., Simard, M., and Tung, W.: Nasadem Global Elevation Model: Methods and Progress, *Int Arch Photogramm*, 41, 125-128, <https://doi.org/10.5194/isprsarchives-XLI-B4-125-2016>, 2016.
- Crompton, J. W., Flowers, G. E., and Stead, D.: Bedrock Fracture Characteristics as a Possible Control on the Distribution of Surge-Type Glaciers, *Journal of Geophysical Research: Earth Surface*, 123, 853-873, <https://doi.org/10.1002/2017JF004505>, 2018.
- Dehecq, A., Gourmelen, N., Gardner, A. S., Brun, F., Goldberg, D., Nienow, P. W., Berthier, E., Vincent, C., Wagnon, P., and Trouvé, E.: Twenty-first century glacier slowdown driven by mass loss in High Mountain Asia, *Nat Geosci*, 12, 22-27, <https://doi.org/10.1038/s41561-018-0271-9>, 2019.
- Farinotti, D., Immerzeel, W. W., de Kok, R. J., Quincey, D. J., and Dehecq, A.: Manifestations and mechanisms of the Karakoram glacier Anomaly, *Nat Geosci*, 13, 8-16, <https://doi.org/10.1038/s41561-019-0513-5>, 2020.
- Gao, Y. P., Liu, S. Y., Wang, J. L., Yao, X. J., Qi, M. M., Liang, P. B., Mu, J. X., Ma, X. G., Zhu, Y., Xie, F. M., Jiang, Z. L., and Zhang, Z.: Characteristics of Musta Glacier surges and their responses to climate change between 1976 and 2023, *Advances in Climate Change Research*, <https://doi.org/10.1016/j.accre.2024.12.007>, 2024.
- Guo, W., Zhang, Z., Wu, K., Liu, S., Shanguan, D., Xu, J., Jiang, Z., and Wang, X.: A review on the advances in surge-type glacier study, *Journal of Glaciology and Geocryology*, 44, 954-970, <https://doi.org/10.7522/j.issn.1000-0240.2022.0091>, 2022.
- Hewitt, K.: The Karakoram anomaly? Glacier expansion and the 'elevation effect,' *Karakoram Himalaya, Mt Res Dev*, 25, 332-340, [https://doi.org/10.1659/0276-4741\(2005\)025\[0332:Tkagea\]2.0.Co;2](https://doi.org/10.1659/0276-4741(2005)025[0332:Tkagea]2.0.Co;2), 2005.
- Huang, Q., Long, D., Du, M. D., Zeng, C., Li, X. D., Hou, A. Z., and Hong, Y.: An improved approach to monitoring Brahmaputra River water levels using retracked altimetry data, *Remote Sens Environ*, 211, 112-128, <https://doi.org/10.1016/j.rse.2018.04.018>, 2018.
- Hugonnet, R., McNabb, R., Berthier, E., Menounos, B., Nuth, C., Girod, L., Farinotti, D., Huss, M., Dussaillant, I., Brun, F., and Kaab, A.: Accelerated global glacier mass loss in the early twenty-first century, *Nature*, 592, 726-731, <https://doi.org/10.1038/s41586-021-03436-z>, 2021.
- Huss, M.: Density assumptions for converting geodetic glacier volume change to mass change, *Cryosphere*, 7, 877-887, <https://doi.org/10.5194/tc-7-877-2013>, 2013.
- Hwang, C., Wei, S. H., Cheng, Y. S., Abulaitijiang, A., Andersen, O. B., Chao, N. F., Peng, H. Y., Tseng, K. H., and Lee, J. C.: Glacier and lake level change from TOPEX-series and Cryosat-2 altimeters in Tanggula: Comparison with satellite imagery, *Terr Atmos Ocean Sci*, 32, 1-20, <https://doi.org/10.3319/Tao.2020.11.15.01>, 2021.



- Jiang, Z. L., Wu, K. P., Liu, S. Y., Wang, X., Zhang, Y., Tahir, A. A., and Long, S. C.: Surging dynamics of South Rimo Glacier, Eastern Karakoram, *Environ Res Lett*, 16, 114044, <https://doi.org/10.1088/1748-9326/ac3175>, 2021.
- Kääb, A., Leinss, S., Gilbert, A., Buhler, Y., Gascoïn, S., Evans, S. G., Bartelt, P., Berthier, E., Brun, F., Chao, W. A., Farinotti, D., Gimbert, F., Guo, W. Q., Huggel, C., Kargel, J. S., Leonard, G. J., Tian, L. D., Treichler, D., and Yao, T. D.: Massive collapse of two glaciers in western Tibet in 2016 after surge-like instability, *Nat Geosci*, 11, 114-120, <https://doi.org/10.1038/s41561-017-0039-7>, 2018.
- 695 Kamb, B., Raymond, C. F., Harrison, W. D., Engelhardt, H., Echelmeyer, K. A., Humphrey, N., Brugman, M. M., and Pfeffer, T.: Glacier Surge Mechanism - 1982-1983 Surge of Variegated Glacier, Alaska, *Science*, 227, 469-479, <https://doi.org/10.1126/science.227.4686.469>, 1985.
- 700 Kumar, A., Negi, H. S., Kumar, K., Shekhar, C., and Kanda, N.: Quantifying mass balance of East-Karakoram glaciers using geodetic technique, *Polar Sci*, 19, 24-39, <https://doi.org/10.1016/j.polar.2018.11.005>, 2019.
- Leclercq, P. W., Kääb, A., and Altena, B.: Brief communication: Detection of glacier surge activity using cloud computing of Sentinel-1 radar data, *Cryosphere*, 15, 4901-4907, <https://doi.org/10.5194/tc-15-4901-2021>, 2021.
- Lei, Y., Gardner, A., and Agram, P.: Autonomous Repeat Image Feature Tracking (autoRIFT) and Its Application for Tracking Ice Displacement, *Remote Sens-Basel*, 13, 749, <https://doi.org/10.3390/rs13040749>, 2021.
- 705 Li, G., Chen, Z. Q., Mao, Y. T., Yang, Z. B., Chen, X., and Cheng, X.: Different glacier surge patterns revealed by Sentinel-2 imagery derived quasi-monthly flow velocity at west Kunlun Shan, Karakoram, Hindu Kush and Pamir, *Remote Sens Environ*, 311, 114298, <https://doi.org/10.1016/j.rse.2024.114298>, 2024.
- Li, X., Long, D., Huang, Q., and Zhao, F.: The state and fate of lake ice thickness in the Northern Hemisphere, *Science Bulletin*, 537-546, <https://doi.org/10.1016/j.scib.2021.10.015>, 2021.
- 710 Li, X. D., Long, D., Cui, Y. H., Liu, T. X., Lu, J., Hamouda, M. A., and Mohamed, M. M.: Ice thickness and water level estimation for ice-covered lakes with satellite altimetry waveforms and backscattering coefficients, *Cryosphere*, 17, 349-369, <https://doi.org/10.5194/tc-17-349-2023>, 2023.
- Lin, R. S., Mei, G., and Xu, N. X.: Accurate and automatic mapping of complex debris-covered glacier from remote sensing imagery using deep convolutional networks, *Geol J*, 58, 2254-2267, <https://doi.org/10.1002/gj.4615>, 2023.
- 715 López, L. A., Gardner, A. S., Greene, C. A., Kennedy, J. H., Liukis, M., Fahnestock, M. A., Scambos, T., and Fahnestock, J. R.: ITS_LIVE: A Cloud-Native Approach to Monitoring Glaciers From Space, *Comput Sci Eng*, 25, 49-56, <https://doi.org/10.1109/Mcse.2023.3341335>, 2023.
- Lovell, H. and Muhammad, S.: Multiple phases of ice-dammed lake formation and drainage associated with a surge of Shisper Glacier, western Karakoram, *J Glaciol*, 71, e10, <https://doi.org/10.1017/jog.2024.80>, 2024.
- 720 Millan, R., Mouginot, J., Rabatel, A., and Morlighem, M.: Ice velocity and thickness of the world's glaciers, *Nat Geosci*, 15, 124-129, <https://doi.org/10.1038/s41561-021-00885-z>, 2022.
- Muñoz-Sabater, J., Dutra, E., Agustí-Panareda, A., Albergel, C., Arduini, G., Balsamo, G., Boussetta, S., Choulga, M., Harrigan, S., Hersbach, H., Martens, B., Miralles, D. G., Piles, M., Rodríguez-Fernández, N. J., Zsoter, E., Buontempo, C.,



- 725 and Thépaut, J. N.: ERA5-Land: a state-of-the-art global reanalysis dataset for land applications, *Earth Syst Sci Data*, 13, 4349-4383, <https://doi.org/10.5194/essd-13-4349-2021>, 2021.
- Nilsson, J., Gardner, A., and Paolo, F.: MEASUREs ITS_LIVE Antarctic Grounded Ice Sheet Elevation Change, Version 1, NASA National Snow and Ice Data Center Distributed Active Archive Center [dataset], <https://doi.org/10.5067/L3LSVDZS15ZV>, 2023.
- 730 Nuth, C. and Kaab, A.: Co-registration and bias corrections of satellite elevation data sets for quantifying glacier thickness change, *Cryosphere*, 5, 271-290, <https://doi.org/10.5194/tc-5-271-2011>, 2011.
- Otsu, N.: A Threshold Selection Method from Gray-Level Histograms, *IEEE Transactions on Systems, Man, and Cybernetics*, 9, 62-66, <https://doi.org/10.1109/TSMC.1979.4310076>, 1979.
- Paul, F., Bolch, T., Briggs, K., Kaab, A., McMillan, M., McNabb, R., Nagler, T., Nuth, C., Rastner, P., Strozzi, T., and
735 Wuite, J.: Error sources and guidelines for quality assessment of glacier area, elevation change, and velocity products derived from satellite data in the Glaciers_cci project, *Remote Sens Environ*, 203, 256-275, <https://doi.org/10.1016/j.rse.2017.08.038>, 2017.
- Pfeffer, W. T., Arendt, A. A., Bliss, A., Bolch, T., Cogley, J. G., Gardner, A. S., Hagen, J. O., Hock, R., Kaser, G., Kienholz, C., Miles, E. S., Moholdt, G., Molg, N., Paul, F., Radic, V., Rastner, P., Raup, B. H., Rich, J., Sharp, M. J., Andeassen, L. M.,
740 Bajracharya, S., Barrand, N. E., Beedle, M. J., Berthier, E., Bhambri, R., Brown, I., Burgess, D. O., Burgess, E. W., Cawkwell, F., Chinn, T., Copland, L., Cullen, N. J., Davies, B., De Angelis, H., Fountain, A. G., Frey, H., Giffen, B. A., Glasser, N. F., Gurney, S. D., Hagg, W., Hall, D. K., Haritashya, U. K., Hartmann, G., Herreid, S., Howat, I., Jiskoot, H., Khromova, T. E., Klein, A., Kohler, J., Konig, M., Kriegel, D., Kutuzov, S., Lavrentiev, I., Le Bris, R., Li, X., Manley, W. F., Mayer, C., Menounos, B., Mercer, A., Mool, P., Negrete, A., Nosenko, G., Nuth, C., Osmonov, A., Pettersson, R.,
745 Racoviteanu, A., Ranzi, R., Sarikaya, M. A., Schneider, C., Sigurdsson, O., Sirguey, P., Stokes, C. R., Wheate, R., Wolken, G. J., Wu, L. Z., Wyatt, F. R., and Consortium, R.: The Randolph Glacier Inventory: a globally complete inventory of glaciers, *J Glaciol*, 60, 537-552, <https://doi.org/10.3189/2014JG13J176>, 2014.
- Quincey, D. J., Glasser, N. F., Cook, S. J., and Luckman, A.: Heterogeneity in Karakoram glacier surges, *J Geophys Res-Earth*, 120, 1288-1300, <https://doi.org/10.1002/2015jf003515>, 2015.
- 750 Ray, R., Zelensky, N., Lemoine, F., Brown, S., Desai, S., and Mitchum, G.: Integrated Multi-Mission Ocean Altimeter Data for Climate Research TOPEX/Poseidon, Jason-1, 2, & 3 User's Handbook Version 5.2, <https://doi.org/10.5067/ALTTS-TJA52>, 2024.
- Schröder, L., Horwath, M., Dietrich, R., Helm, V., van den Broeke, M. R., and Ligtenberg, S. R. M.: Four decades of Antarctic surface elevation changes from multi-mission satellite altimetry, *Cryosphere*, 13, 427-449, <https://doi.org/10.5194/tc-13-427-2019>, 2019.
- 755 Shi, Y. L., Liu, G. X., Wang, X. W., Liu, Q., Zhang, R., and Jia, H. G.: Assessing the Glacier Boundaries in the Qinghai-Tibetan Plateau of China by Multi-Temporal Coherence Estimation with Sentinel-1A InSAR, *Remote Sens-Basel*, 11, 392, <https://doi.org/10.3390/rs11040392>, 2019.



- Smith, B., H. A. Fricker, A. Gardner, M. R. Siegfried, S. Adusumilli, B. M. Csathó, N. Holschuh, J. Nilsson, F. S. Paolo, &
760 the ICESat-2 Science Team: ATLAS/ICESat-2 L3A Land Ice Height (3), NASA National Snow and Ice Data Center
Distributed Active Archive Center [dataset], <https://doi.org/10.5067/ATLAS/ATL06.003>, 2020.
- Surazakov, A. and Aizen, V.: Positional Accuracy Evaluation of Declassified Hexagon KH-9 Mapping Camera Imagery,
Photogramm Eng Rem S, 76, 603-608, <https://doi.org/10.14358/Pers.76.5.603>, 2010.
- Tao, D. L., Cheng, Y. S., Hwang, C., Sun, W. K., and Lee, H.: The Rise and Fall of Alaska and Yukon Glaciers Detected by
765 TOPEX/Poseidon and Jason-2 Altimeters Using a Novel Glacier-Threshold Method, *J Geophys Res-Earth*, 128,
[e2022JF006977](https://doi.org/10.1029/2022JF006977), <https://doi.org/10.1029/2022JF006977>, 2023.
- Truffer, M., Kääh, A., Harrison, W. D., Osipova, G. B., Nosenko, G. A., Espizua, L., Gilbert, A., Fischer, L., Huggel, C.,
Craw Burns, P. A., and Lai, A. W.: Chapter 13 - Glacier surges, in: *Snow and Ice-Related Hazards, Risks, and Disasters*
(Second Edition), edited by: Haeberli, W., and Whiteman, C., Elsevier, 417-466, [https://doi.org/10.1016/B978-0-12-817129-](https://doi.org/10.1016/B978-0-12-817129-5.00003-2)
770 [5.00003-2](https://doi.org/10.1016/B978-0-12-817129-5.00003-2), 2021.
- Wu, K. P., Liu, S. Y., Jiang, Z. L., Xu, J. L., Wei, J. F., and Guo, W. Q.: Recent glacier mass balance and area changes in the
Kangri Karpo Mountains from DEMs and glacier inventories, *Cryosphere*, 12, 103-121, [https://doi.org/10.5194/tc-12-103-](https://doi.org/10.5194/tc-12-103-2018)
2018, 2018.
- Wu, K. P., Liu, S. Y., Jiang, Z. L., Liu, Q., Zhu, Y., Yi, Y., Xie, F. M., Tahir, A. A., and Saifullah, M.: Quantification of
775 glacier mass budgets in the Karakoram region of Upper Indus Basin during the early twenty-first century, *J Hydrol*, 603,
[127095](https://doi.org/10.1016/j.jhydrol.2021.127095), <https://doi.org/10.1016/j.jhydrol.2021.127095>, 2021.
- Wu, K. P., Liu, S. Y., Jiang, Z. L., Zhu, Y., Xie, F. M., Gao, Y. P., Yi, Y., Tahir, A. A., and Muhammad, S.: Surging
Dynamics of Glaciers in the Hunza Valley under an Equilibrium Mass State since 1990, *Remote Sens-Basel*, 12, 2922,
<https://doi.org/10.3390/rs12182922>, 2020.
- 780 Wytiahlowsky, H., Stokes, C. R., and Evans, D. J. A.: Remote sensing of glacier change (1965-2021) and identification of
surge-type glaciers on Severnaya Zemlya, Russian High Arctic, *J Glaciol*, 69, 1764-1784,
<https://doi.org/10.1017/jog.2023.60>, 2023.
- Xie, F. M., Liu, S. Y., Gao, Y. P., Zhu, Y., Bolch, T., Kääh, A., Duan, S. M., Miao, W. F., Kang, J. F., Zhang, Y. N., Pan, X.
R., Qin, C. X., Wu, K. P., Qi, M. M., Zhang, X. H., Yi, Y., Han, F. Z., Yao, X. J., Liu, Q., Wang, X., Jiang, Z. L., Shangguan,
785 D. H., Zhang, Y., Grünwald, R., Adnan, M., Karki, J., and Saifullah, M.: Interdecadal glacier inventories in the Karakoram
since the 1990s, *Earth Syst Sci Data*, 15, 847-867, <https://doi.org/10.5194/essd-15-847-2023>, 2023.
- Yang, J. R., Jiang, Z. L., Liu, S. Y., Wang, X., Zhang, Y., Zhang, Z., and F., W. J.: Characteristics of recent surging of
Kunchhang Glacier, East Karakoram, *Journal of Glaciology and Geocryology*, 43, 1732-1745,
<https://doi.org/10.7522/j.issn.1000-0240.2021.0063>, 2021.
- 790 Yu, Z. G., Zhang, G. H., Zhang, C. X., Zhang, Z. P., and Wang, Q. B.: PySide-based Time-Series InSAR processing
visualization and experimental application for deformation monitoring, *Engineering of Surveying and Mapping*, 33, 41-48,
<https://doi.org/10.19349/j.cnki.issn1006-7949.2024.06.006>, 2024.



- Zhang, Z. J., Ahmad, Z., Xiong, S. Q., and Zhang, W. C.: Glacier velocity and surge detection in the Karakoram region, Pakistan: using remotely sensed data with cross-correlation feature tracking, *Int J Digit Earth*, 17, 2441928, 795 <https://doi.org/10.1080/17538947.2024.2441928>, 2024.
- Zhao, F. Y., Long, D., Li, X. D., Huang, Q., and Han, P. F.: Rapid glacier mass loss in the Southeastern Tibetan Plateau since the year 2000 from satellite observations, *Remote Sens Environ*, 270, 112853, <https://doi.org/10.1016/j.rse.2021.112853>, 2022.
- Zhou, Y. S., Li, Z., and Li, J.: Slight glacier mass loss in the Karakoram region during the 1970s to 2000 revealed by KH-9 800 images and SRTM DEM, *J Glaciol*, 63, 331-342, <https://doi.org/10.1017/jog.2016.142>, 2017.